https://doi.org/10.5194/egusphere-2026-362
Preprint. Discussion started: 10 March 2026

Conservation of Heat in the Coupled Arctic Prediction System (CAPS v1.1): Comprehensive model evaluation based on the MOSAiC observations

Chao-Yuan Yang[1], Fengguan Gu[1], Jiping Liu[1], Annette Rinke[2], Hu Yang[1], Xiaoxu Shi[1]

[1]Southern Marine Science and Engineering Guangdong Laboratory (Zhuhai) and School of Atmospheric Sciences, Sun Yat-sen University, Zhuhai, Guangdong, China

[2]Alfred Wegener Institute, Helmholtz Centre for Polar and Marine Research, Potsdam, Germany

Corresponding authors:

Fengguan Gu (gufg3@mail.sysu.edu.cn) and Jiping Liu (liujp63@mail.sysu.edu.cn)

https://doi.org/10.5194/egusphere-2026-362
Preprint. Discussion started: 10 March 2026

Abstract

Atmosphere–sea ice–ocean interactions are vital to understand past and future changes of Arctic climate system. It is essential to ensure the energy closure across model components to investigate these interactions with coupled models at longer timescales. Here, we present the improved version of Coupled Arctic Prediction System (CAPS) with the conservation of heat fluxes exchanged between the atmosphere (WRF) and ocean-sea ice (ROMS-CICE) components. A set of pan-Arctic simulations covering the period of Multidisciplinary drifting Observatory for the Study of Arctic Climate (MOSAiC) was conducted with the improved CAPS. The improved CAPS significantly reduces the inconsistency in heat flux exchange between WRF and ROMS-CICE, leading to better performance in simulating Arctic sea ice conditions compared with satellite observations than its predecessor showing the drifting behaviors. The model capability of CAPS to simulate the atmosphere, ocean, and sea ice conditions in the Arctic climate system were also evaluated based on the comprehensive observations obtained from the MOSAiC drift. The assessments indicate that CAPS reproduces reasonable evolutions of Arctic conditions along the track of MOSAiC observations but accompanies with biases contributed by simulated synoptic storm systems. By applying the spectral nudging technique in the upper atmospheric levels, CAPS can better replicate the observed storm systems and reduce biases shown in the free simulation. The evaluations shown in this article also highlight the key areas for further investigations in CAPS (as well as in other numerical prediction systems) including atmospheric boundary layer processes (surface turbulent heat fluxes) and cloud processes in polar regions.

https://doi.org/10.5194/egusphere-2026-362
Preprint. Discussion started: 10 March 2026

1. Introduction

Arctic, a climate system experiencing drastic changes, has undergone a transition to a new state. Arctic sea ice extent (SIE) has been decreasing with rates of -0.52 (annual-mean), -0.37 (March-mean), and -0.78 (September-mean) million km^2 per decade over the period of 1979-2024 (Meier et al., 2024; Roach and Meier, 2025). The decline of summer SIE also exhibits a mixture of different rates with the faster period of 1992-2006 (-0.99 million km^2 per decade) and the slowed-down period of 2007-2021 (-0.07 million km^2 per decade) (Polyakov et al., 2023). Arctic sea ice thickness (SIT) has also decreased from a peak of 3.6 m (winter) / 2.7 m (fall) in 1980 to 2 m / 1.3 m in recent years, which is largely a result of multi-year ice coverage replaced by first-year ice coverage (Kacimi and Kwok, 2024). Corresponding to the slowed-down of summer SIE decline, satellite records also show near-negligible thickness trends since 2007.

In addition to dramatics changes in sea ice properties, near-surface air temperature in the Arctic region is warming three to four times faster than the global average, a phenomenon known as Arctic amplification related to sea ice changes (Holland and Bitz, 2003, Rantanen et al., 2022; Screen and Simmonds, 2010). Over the past two decades, the Arctic Ocean, specifically in the Beaufort Gyre region, has shown a notable accumulation of freshwater (e.g., Timmermans and Toole, 2023), which is associated with sea ice decline and wind strengthening (e.g., Giles et al., 2012; Wang et al., 2025). Besides of the increases of freshwater content in the Beaufort Gyre, sea ice decline also plays a role in recent warming of Atlantic Water layer in the Arctic Eurasian basin, a phenomenon known as Arctic atlantification (Polyakov et al.,

https://doi.org/10.5194/egusphere-2026-362
Preprint. Discussion started: 10 March 2026

2017; Wang et al., 2024). Changes in the Arctic described above may also have wider impacts outside of the Arctic, such as extreme weather events in mid-latitude (e.g., Cohen et al., 2014; 2020), and the releasing of freshwater from the Beaufort Gyre into the North Atlantic influencing the Atlantic Meridional Overturning Circulation (e.g., Zhang et al., 2021). Accurately simulating Arctic sea ice and climate is crucial due to profound impacts of the Arctic on regional weather and climate patterns, and ocean dynamics.

Previously, we developed a Coupled Arctic Prediction System (CAPS; Yang et al., 2020; 2022) designated for seasonal Arctic sea ice and climate prediction. Experimental seasonal Arctic sea ice predictions conducted in Yang et al. (2020; 2022) have demonstrated that CAPS has the potential to provide skillful Arctic sea ice predictions at seasonal timescales. Despite the promising performance of CAPS in seasonal sea ice predictions, CAPS nevertheless does not fully consider the energy closure between the atmosphere and ocean components through surface heat fluxes, which prevents the applications of CAPS for longer timescales, such as the COordinated Regional Climate Downscaling EXperiment (CORDEX; Gutowski et al., 2016). Discontinuities in surface fluxes and/or numerical errors, which disrupt the conservation of heat or moisture across components in the earth system (e.g., Liepert and Previdi 2012; Lucarini and Ragone 2011; Rahmstorf, 1995), are key factors for the issue of climate drift in climate models (e.g., Irving et al., 2021; Sen Gupta et al., 2013). Atmosphere–sea ice–ocean interactions through variations in surface fluxes are also crucial for climate variability in Arctic sea ice cover (e.g., Deng and Dai, 2019), and remote impacts of Arctic sea ice on El Niño–Southern Oscillation (e.g., Deng and Dai, 2024; Liu et al., 2022).

https://doi.org/10.5194/egusphere-2026-362
Preprint. Discussion started: 10 March 2026

Recently, a year-long polar expedition called the Multidisciplinary drifting Observatory for the Study of Arctic Climate (MOSAiC; Nicolaus et al., 2022; Rabe et al., 2022; Shupe et al., 2022) was the first year-round expedition into the central Arctic ice pack observing the atmosphere, sea ice, snow, and oceanic physical, chemical, and biological properties in the Arctic climate system from September 2019 to October 2020 with Research Vessel Polarstern (Knust, 2017). The MOSAiC campaign took place 22 years after the previous year-long polar expedition called the Surface Heat Budget of the Arctic campaign (SHEBA; Uttal et al., 2002). Different from SHEBA taking place over multiyear sea ice, MOSAiC was over thinner and more dynamic first-year sea ice aiming to increase our understandings of the coupled Arctic climate system under global climate change, and to improve the representations of Arctic climate system within climate models.

In this paper, we present an improved version of CAPS by minimizing the inconsistency of surface heat fluxes between the atmosphere, sea ice, and ocean components and compared the simulation results with those produced by the previous version of CAPS. Taking advantage of comprehensive observations obtained during the MOSAiC expedition, we evaluate the capabilities of the improved CAPS in reproducing Arctic climate system including sea ice, atmosphere, and ocean during the MOSAiC period. This paper is structured as follows. Section 2 provides an overview of CAPS focusing on the coupling approach, describes the design of numerical experiments and the model configurations for the model evaluation, and the data measured throughout the MOSAiC campaign. Section 3 presents the evaluation of improved CAPS based on satellite-observed sea ice conditions and the MOSAiC observations.

https://doi.org/10.5194/egusphere-2026-362
Preprint. Discussion started: 10 March 2026

Concluding remarks and discussions are provided in section 4.

2. Methods and Data

2.1. Coupled Arctic Prediction System

CAPS consists of the Weather Research and Forecasting Model (WRF version 4.1.2), the Regional Ocean Modeling System (ROMS version 3.8), and the Community Ice CodE (CICE version 6.0.0). The data exchange between WRF and ROMS is achieved by the Model Coupling Toolkit (MCT; Larson et al., 2005). Instead of exchanging data through MCT, CICE is embedded within ROMS as subroutines. The integrated ROMS and CICE use the same model time step to better reflect that temperature and salinity of the surface layer will be instantaneously adjusted under supercooled conditions in ROMS, and the freezing/melting potential is calculated accordingly for CICE to form/melt sea ice (adapted from Smith et al., 2010). The required forcing variables of CICE held by ROMS and the CICE-derived variables to ROMS are exchanged through the ROMS-CICE internal coupler every oceanic/sea ice time step. All model components of CAPS use the same horizontal model grid so that the data exchange between model components does not involve horizontal interpolation.

2.1.1. Original coupling approach

Turbulent heat fluxes of ice-covered ocean cells in WRF and ROMS are based on the mosaic method:

$$F = (1 - A_{ice}) \times F_{ao} + A_{ice} \times F_{ai/io} \quad (1)$$

where F is the summed turbulent heat flux for driving the boundary layer physics in WRF or as the vertical boundary conditions in ROMS, F_{ao} is turbulent heat flux at the atmosphere–

https://doi.org/10.5194/egusphere-2026-362
Preprint. Discussion started: 10 March 2026

ocean interface, $F_{ai/io}$ is turbulent heat flux at the atmosphere–ice or the ice–ocean interface, and A_{ice} is sea ice concentration. Figure 1 shows the schematic of turbulent heat flux calculation in CAPS. In the ROMS side, F_{io} is provided by CICE based on a Rossby similarity law (Maykut and McPhee, 1995) and F_{ao} is based on the Coupled Ocean–Atmosphere Response Experiment (COARE) 3.0 bulk formula (Fairall et al., 2003). In the WRF side, F_{ai} is computed by the Noah land surface physics (Chen and Dudhia, 2001) and F_{ao} is calculated by the COARE 3.0 algorithm. However, CICE calculates its own F_{ai} with a stability-based boundary parameterization (Jordan et al., 1999). Also, WRF and ROMS do not share the same modifications for implementing the COARE 3.0 algorithm. In other words, the heat flux inconsistency exists at the WRF–ROMS/CICE interface in the original CAPS (Fig. 1a).

2.1.2. Revised coupling approach

To address the inconsistency in turbulent heat flux calculation within CAPS, only one model component is designated to calculate turbulent heat fluxes for all interfaces (Fig. 1b), i.e., turbulent heat flux calculations at the atmosphere–ice and atmosphere–ocean interfaces are revised. Specifically, WRF determines turbulent heat fluxes at the atmosphere–ocean interface based on the COARE 3.0 parameterization for ROMS to receive. Turbulent heat fluxes at the atmosphere–ice interface are calculated in CICE based on wind fields, potential temperature, and specific humidity of the lowest atmospheric level, and the corresponding height from WRF (see Table 1), and CICE-derived heat fluxes are transferred to WRF.

In addition to turbulent heat fluxes, the related variables (i.e., surface temperature, albedo, and emissivity) participating in the radiation physics in WRF also use the same mosaic

https://doi.org/10.5194/egusphere-2026-362
Preprint. Discussion started: 10 March 2026

approach as in Eq. (1) for ice-covered cells. Both WRF and ROMS use 0.06 as the ocean surface albedo. As for the ice surface albedo, the delta-Eddington scheme in CICE determines the absorption of downward shortwave radiation at the ice surface (Briegleb and Light, 2007), which influences the ice surface albedo diagnostic. However, the original ice surface albedo diagnostic based on the delta-Eddington scheme occasionally returns out of bound values (i.e., larger than one), and zero ice surface albedo in case of zero downward shortwave radiation (e.g., polar night regions). The following approach is applied in CICE to provide full coverage of ice surface albedo, α_{ice}, to WRF:

$$\alpha_{ice} = \begin{cases} (F_{swdn} - F_{swabs})/F_{swdn} & if\ F_{swdn} > 0 \\ \alpha_{ccsm} & if\ F_{swdn} = 0 \end{cases} \quad (2)$$

where F_{swdn} is the downward shortwave radiation from WRF, F_{swabs} is the ice-absorbed shortwave radiation based on the delta-Eddington scheme, and α_{ccsm} is the diagnostic albedo based on the parameterization used in the Community Climate System Model, which is the function of snow/ice surface temperature, ice thickness, snow thickness, and the spectrum of downward shortwave radiation. The surface emissivity of ocean, 0.984, is used for both WRF and ROMS (Konda et al., 1994), and WRF uses the same value (0.95) as in CICE for the surface emissivity of snow and ice. Warren (2019) reported that ice surface emissivity is 0.92 and snow surface emissivity is 0.98-0.99. Table 1 summarizes the variables that WRF, ROMS, and CICE exchange through the couplers with the improved coupling approach. The variables exchange with the original coupling approach are also summarized in Table S1 in the supplement.

2.1.3. Coupling cycle

The model sequence of each model component in the CAPS based on the revised coupling

https://doi.org/10.5194/egusphere-2026-362
Preprint. Discussion started: 10 March 2026

approach is illustrated in Figure 2. In our implementation of the revised coupling in CAPS, WRF calculates its physical processes for the first atmospheric time step to determine all variables (see Table 1), before the initial data exchange between WRF and ROMS/CICE, which provides non-zero values for precipitation and downward radiative heat fluxes to drive ROMS/CICE physics until the next data exchange. Originally, the surface layer scheme in WRF updates the values of ice surface (e.g., surface temperature and turbulent heat fluxes). In our implementation, the surface layer scheme still updates the related variables of ice surface to maintain the stability of WRF, but the summed values based on Eq. (1) with the CICE-derived values (turbulent heat fluxes of ice surface, ice surface temperature, and ice surface albedo) are the final output values for the boundary layer scheme and the radiation transfer scheme in WRF.

After receiving values from WRF, ROMS will determine the net heat (net radiative heat fluxes plus turbulent heat fluxes), net salt (evaporation minus precipitation), and momentum fluxes of the ocean surface assuming grid cells are ice-free. Subsequently, CICE receives its required variables (see Table 1) through the ROMS-CICE internal coupler, computes fluxes at the atmosphere–ice and ice–ocean interfaces, and then updates ice state variables to the next sea ice time step. The computed heat, water, salt, and momentum fluxes at the ice–ocean interface are integrated with the fluxes of ocean surface calculated previously based on Eq. (1) as the final top boundary conditions for ROMS to update its state variables to the next oceanic time step.

As described in Section 2.1, the same horizontal model grid for all model components in

https://doi.org/10.5194/egusphere-2026-362
Preprint. Discussion started: 10 March 2026

CAPS makes WRF demand more computational resources than ROMS/CICE. WRF is also more restrictive in atmospheric time step compared to ROMS. To balance the computational loading between WRF and ROMS/CICE, WRF is configured to integrate more atmospheric time steps before exchanging data with ROMS/CICE in this study, and WRF exchanges data with ROMS/CICE every oceanic/sea ice time step (Fig. 2, Tab. 2, and see Sect. 2.2 for the exact setup). Note that all data exchanges are done with instantaneous fields without employing time averaging over a coupling cycle in this study.

2.2. Model configurations and simulation designs

In this study, the model domains of WRF, ROMS, and CICE is the same as the previous pan-Arctic configurations of CAPS (Yang et al., 2022; 2024, and see Fig. S1). The domain includes 320 x- and 440 y- grid points with ~24km horizontal resolution on the polar stereographic projection. Initial and lateral boundary conditions for WRF are generated from the fifth generation of European Centre for Medium-Range Weather Forecasts Reanalysis (ERA5, Hersbach et al., 2023, last access: 30 Nov 2025), with 6-hourly time spacing and a spatial resolution of 0.25 degrees. During the initialization processes of WRF, we specify the initial top of lowest model layer to 10 m, which provides ~5 m for the height of the lowest model layer (z_a, see Table 1), and the remaining model layers (50 layers in total, see Table 2) are determined by the default stretching parameters. Global Ocean Ensemble Physics Reanalysis (GREP) produced by Copernicus Marine Service (https://doi.org/10.48670/moi-00024, last access: 30 Nov 2025) is utilized to create initial and lateral boundary conditions for ROMS and CICE. The ensemble of GREP includes Global Ocean ReanalYses and Simulations

https://doi.org/10.5194/egusphere-2026-362
Preprint. Discussion started: 10 March 2026

(GLORYS2V4), Ocean Reanalysis System 5 (ORAS5), and the CMCC Global Ocean Reanalysis Systems (C-GLORSv7). GREP provides daily mean oceanic and sea ice states with a spatial resolution of 0.25 degrees, and the ensemble mean is used for ROMS and CICE. Previous studies have shown that GREP can provide reasonable estimates of sea ice and oceanic states in the Arctic (Cocetta et al., 2024; Yao et al., 2025).

In this study, two numerical experiments covering the entire period of MOSAiC expedition, starting from 00 UTC September 1st, 2019, to 00 UTC November 1st, 2020 have been conducted for the model evaluation, and two experiments differ in whether the spectral nudging scheme is applied in WRF. As shown in Cassano et al. (2011), the stand-alone WRF simulations on the pan-Arctic domain tend to have significant biases in atmospheric circulation due to improper treatment of stratosphere and the model top boundary. The nudged experiment applies the spectral nudging to the wind, temperature, and humidity fields with wavenumber 1 to 3 nudged horizontally, and the spectral nudging is only applied to the top 25 of the 50 model vertical layers (above ~6.7 km height) with the 10-layer transition (26 to 35 model layer) zone from zero to full nudging weight (0.0003 s^{-1}). Hereafter, experiments without and with the spectral nudging are denoted as Exp_FREE and Exp_NUD. Physical options of each model component are mostly identical to those used in Yang et al. (2024) with several differences for the revised CAPS. For shortwave and longwave radiation, the Rapid Radiative Transfer Model (RRTMG, Iacono et al., 2008) is utilized as the radiation transfer scheme in WRF. The vertical tracer mixing scheme in ROMS is changed to the Large-McWilliams-Doney interior closure scheme, also known as K-profile parameterization (KPP, Large et al., 1994) with several

https://doi.org/10.5194/egusphere-2026-362
Preprint. Discussion started: 10 March 2026

compiling options (controlled by C-preprocessor keywords) activated in ROMS including surface boundary layer mixing (LMD_SKPP), bottom boundary layer mixing (LMD_BKPP, Durski et al., 2004), non-local transport (LMD_NONLOCAL), convective mixing due to shear instability (LMD_CONVEC), double-diffusive mixing (LMD_DDMIX), the effect of shear instability on diffusivity (LMD_RIMIX), and Shapiro filter to boundary layer depth (LMD_SHAPIRO, Shapiro 1970). Further details of physics options and experiment configurations are summarized in Table 2. To investigate the consistency of surface heat flux budget between WRF and ROMS/CICE, an additional experiment using the same configuration as Exp_FREE is conducted with the original CAPS (Fig. 1a) and denoted as Exp_FREE_OLD.

2.3. Evaluation data

2.3.1. MOSAiC data

To evaluate the performance of the revised CAPS, the observations from the MOSAiC expedition are utilized, which include radiosondes, the MOSAiC cloud observing suite, meteorological tower, atmospheric surface flux stations (ASFS), conductivity-temperature profiling through depth (CTD) buoys, and snow and ice mass balance array (SIMBA) buoys (Nicolaus et al., 2022; Rabe et al., 2022; Shupe et al., 2022). These observations are distributed within an observational network with approximately 15 km radius, and the network consists of the central site (CO), three large sites (L1, L2, and L3) approximately 15 km away from CO, and eight medium sites (M1 to M8). The distribution of sites during MOSAiC is referred to Fig. 2 of Bliss et al. (2023). For atmospheric observations, radiosondes were launched four

https://doi.org/10.5194/egusphere-2026-362
Preprint. Discussion started: 10 March 2026

times per day, typically at 05, 11, 17, and 23 UTC during MOSAiC. These radiosondes provide vertical profiles from 12 m up to an altitude of about 30 km for temperature, relative humidity, pressure, and winds (Maturilli et al., 2022). The cloud observing suite includes multiple sensors (e.g., cloud radar, depolarization lidar, microwave radiometer, and ceilometer), which provide time-height derivations of cloud microphysical properties (e.g., the cloud type, the condensed water content) (Shupe, 2022). The meteorological tower at Met City (the CO site) measured surface radiative (both downward and upward) heat fluxes with 1-min average intervals. Turbulent heat fluxes were calculated from the tower measurements based on eddy covariance method with 10-min average intervals (Cox et al., 2023). Three ASFS flux measurements, which provide radiative and turbulent fluxes, located at the L1, L2, and L3 sites are also utilized, and these flux measurements will be averaged spatially for the evaluation. For oceanic observations, a set of 8 ice-tethered buoy systems with five CTD units at depths of 10, 20, 50, 75, and 100m observing temperature and salinity with 2-min intervals are chosen (Hoppmann et al., 2022). Note that only the CTD-buoy at the M1 site, which provides long records of temperature and salinity, is used for the evaluation. For sea ice observations, SIT and snow depth measured by SIMBA buoys with 6-hour intervals are used (Lei et al., 2021). SIT can be highly heterogeneous, ranging from a few centimeters to several meters within ~50 km horizontal distance (e.g., Fig. 2.2 of Haas, 2017). SIT observed by the SIMBA buoys can also be different across each buoy due to the spatial heterogeneity of SIT. Also, the SIMBA buoys were not deployed simultaneously during the MOSAiC expedition, and some buoys only provide relatively short records of SIT and snow depth. SIMBA buoys with relatively long

https://doi.org/10.5194/egusphere-2026-362
Preprint. Discussion started: 10 March 2026

temporal coverage are chosen for the average of their shared period (from December 2019 to June 2020) to minimize the spatial heterogeneity of SIT and better match the average state represented by the model cells, and these buoys are located at the CO site with buoy T56, T62, T66, the L1, L2, and L3 sites with buoy T63, T67, T70, and the M4 site with buoy T58. The operational periods of SIMBA buoys during MOSAiC are referred to Fig. 2 of Lei et al. (2022). Daily averages from these measurements will be compared with the grid cell nearest to the observations in the modeled daily mean outputs. The track of the MOSAiC expedition started in the northern Laptev Sea, began to move across the central Arctic with the Transpolar Drift, and finally reached the sea ice edge in Fram Strait (Fig. 1 of Bliss et al., 2023).

2.3.2. Satellite-derived and reanalysis-based sea ice data

Since the data collected during the MOSAiC expedition can only provide point observations along the drift, satellite-derived and reanalysis-based sea ice data are also utilized to evaluate the revised CAPS spatially. For sea ice concentration (SIC), the daily SIC obtained from the National Snow and Ice Data Center (NSIDC) is chosen in this study. The SIC data is measured by Nimbus-7 Scanning Multichannel Microwave Radiometer (SMMR), the Defense Meteorological Satellite Program (DMSP), Special Sensor Microwave/Imagers (SSM/Is), and Special Sensor Microwave Imager/Sounder (SSMIS) passive microwave sensors, and the SIC data is on the NSIDC polar stereographic grid with a spatial resolution of 25 km (NSIDC_0051, DiGirolamo et al., 2022, last access: 30 Nov 2025). For sea ice thickness (SIT), the statistically merged SIT based on CryoSat-2 and Soil Moisture and Ocean Salinity satellite data (CS2SMOS, Ricker et al., 2017, last assess: 30 Nov 2025) is utilized. However, satellite-based

https://doi.org/10.5194/egusphere-2026-362
Preprint. Discussion started: 10 March 2026

SIT is not available during the melting season since satellite cannot differentiate the mixture of wet snow/sea ice, melt ponds, and open water (e.g., Huntemann et al., 2014). The daily SIT produced by the Pan-Arctic Ice Ocean Modeling and Assimilation System (PIOMAS, Zhang and Rothrock, 2003) is chosen to fill the data gap in CS2SMOS.

3. Results

3.1 Evaluation

3.1.1. Evaluation of sea ice concentration and thickness

In this section, we first evaluate the revised CAPS focused on Exp_FREE and Exp_NUD (with Exp_FREE_OLD as reference) against satellite-based sea ice observations to provide an overview of the performance of revised CAPS in simulating sea ice conditions over the pan-Arctic domain during the MOSAiC period. Figure 3 shows the evolutions of SIE of the observations, Exp_FREE, Exp_NUD, and Exp_FREE_OLD, as well as the integrated ice-edge error (IIEE, Goessling et al., 2016) of Exp_FREE, Exp_NUD, and Exp_FREE_OLD with respect to the observations. SIE is computed as the summation of areas of all cells with at least 15% SIC, and the observed SIE is calculated from NSIDC-0051 SIC. IIEE is defined as the sum of areas where the simulation and the observation disagree on SIC of the same cell being above or below 15%. The smaller (larger) IIEE indicates that the simulated distribution of sea ice edges is comparable (different) to the observed distribution. As shown in Fig. 3a, both Exp_FREE and Exp_NUD can reasonably reproduce the seasonal cycle (i.e., the timing of maximum and minimum) of SIE during the MOSAiC period, and both experiments show an underestimation of $1.0\sim1.5 \times 10^6$ km^2 in SIE with respect to the observations around March

https://doi.org/10.5194/egusphere-2026-362
Preprint. Discussion started: 10 March 2026

2020. In general, the evolution of SIE in Exp_FREE (Fig. 3a) shows smaller SIE for 2019/2020 winter months (November 2019 to April 2020) and larger SIE for 2020 summer months (June to October 2020) compared to that in Exp_NUD (Fig. 3a). As reference, Exp_FREE_OLD (Fig. 3a) simulates larger SIE than Exp_FREE, and the differences in SIE become significantly larger in 2020 summer, indicating the original coupling approach used in the previous version of CAPS (Fig. 1a) may prone to drift to a state with extensive sea ice coverage as the model integrates for longer period. IIEE of Exp_NUD (Fig. 3b) is generally smaller than that of Exp_FREE (Fig. 3b) for most of the simulation period, suggesting that Exp_NUD shows better performance in simulating the distribution of sea ice edges than Exp_FREE. Compared with Exp_FREE, Exp_FREE_OLD (Fig. 3b) shows generally smaller IIEE from September 2019 to April 2020 corresponding to better agreement between the simulated SIE in Exp_FREE_OLD and the observed SIE. After July 2020, Exp_FREE_OLD shows generally larger IIEE than Exp_FREE.

The monthly-averaged March and September SIC of the observations in 2020, and the difference between the simulations and the observations are shown in Figure 4. Corresponding to SIE shown in Fig. 3a, the underestimated SIE of Exp_FREE and Exp_NUD in March 2020 are mainly by the ULSIE in both experiments in the Sea of Okhotsk, the Barents Sea, the Labrador Sea, and Davis Strait (Fig. 4b-c). In contrast to better agreement with the observed SIC shown in Exp_NUD (Fig. 4c, colored areas), Exp_FREE simulates larger SIC in the Bering Sea and smaller ice coverage the Barents Sea in the in March 2020 (Fig. 4b). Generally, Exp_FREE_OLD shows larger ice coverage (e.g., the Sea of Okhotsk, the Barents Sea) than

https://doi.org/10.5194/egusphere-2026-362
Preprint. Discussion started: 10 March 2026

Exp_FREE in March 2020 (Fig. 4b, 4d). In September 2020, the similar areal coverage of the OLSIE along coasts of Alaska, central, and eastern Siberia and the ULSIE near the Fram Strait and Canadian Archipelago in Exp_FREE contribute to smaller difference in SIE compared with the observations (Fig. 3a, 4f). In contrast, the ULSIE in the central Arctic Ocean and Canadian Archipelago (which partially compensated by the OLSIE in the Chukchi Sea) is the main contributor to the underestimation of SIE in Exp_NUD (Fig. 3a, 4g). Exp_FREE_OLD shows that most of the Arctic Ocean is covered by ice with at least 15% SIC (Fig. 4h) corresponding to significant overestimation of SIE in summer 2020 shown in Fig. 3a.

Figure 5 shows the monthly-averaged March and September SIT of the reference data and the simulations in 2020. The average SIT of all cells with at least 1% SIC for the reference data and the simulations in March and September 2020 are also shown in Figure S2 in the supplement. In March 2020, all experiments can reproduce the general patterns of SIT compared with CS2SMOS, showing the thickest ice located north of the Canadian Archipelago with decreasing thickness gradient toward Siberia (Fig. 5a-d). However, all experiments show more thicker SIT accumulated in the Western Arctic Ocean, especially along the coastal areas of Alaska and eastern Siberia. Exp_FREE simulates overall thinner SIT (~1.13 m, Fig. S2) in the Arctic Ocean compared with Exp_NUD (~1.16 m, Fig. S2). For regional difference, Exp_NUD show thicker SIT in the north of the Canadian Archipelago and Alaska but thinner SIT along the Siberia coast compared to Exp_FREE (Fig. 5b-c). Corresponding to larger ice coverage of Exp_FREE_OLD in March 2020 (Fig. 4d), Exp_FREE_OLD shows relatively thicker SIT (~1.17 m, Fig. S2) in most of the Arctic Ocean than Exp_FREE (Fig. 5b, 5d). The

https://doi.org/10.5194/egusphere-2026-362
Preprint. Discussion started: 10 March 2026

simulated biases of SIT in September 2020 of both experiments are partly associated with those in March 2020. That is, the thinner SIT along the Siberia coast in Exp_NUD is less persistent, and the thicker SIT along the coastal areas of Alaska and eastern Siberia in Exp_FREE and Exp_NUD in March 2020 is more persistent (Fig. 5b-c, 5f-g). The OLSIE and ULSIE in September 2020 (Fig. 4f-g) are also associated with the simulated bias of SIT in March 2020, such as the OLSIE of Exp_FREE and Exp_NUD in the Chukchi Sea, and the ULSIE of Exp_NUD in the central Arctic Ocean. The evolution of SIT from April 2020 to August 2020 shown in Figure S3 in the supplement also illustrates the lasting influence of simulated bias of SIT in March 2020. Generally, Exp_NUD shows better agreement with CS2SMOS and PIOMAS than Exp_FREE in both March and September 2020 (Fig. 5, Fig. S2). In Exp_FREE_OLD, most of the Arctic Ocean is still covered by sea ice with the average SIT of 1.25 m in summer 2020 (Fig. 5h, Fig. S2), which is significantly thicker than Exp_FREE (~0.54 m, Fig. S2) and Exp_NUD (~0.59 m, Fig. S2), corresponding to extensive ice coverage in most of the Arctic Ocean shown in Fig. 4h.

3.1.2. Evaluation of improved flux coupling

To demonstrate the consistence of flux coupling in the improved CAPS and to investigate how the inconsistency in surface heat flux exchanges between WRF and ROMS/CICE in the original coupling approach (Fig. 1a) contribute to the simulated sea ice biases in Exp_FREE_OLD described above, the differences in the surface heat flux budget components between the WRF and the ROMS/CICE sides (averaged over all open-ocean and ice-covered grid cells, also referred to Fig. 1 and Equ. 1) for Exp_FREE_OLD and Exp_FREE are shown

https://doi.org/10.5194/egusphere-2026-362
Preprint. Discussion started: 10 March 2026

in Figure 6. With the revised coupling approach (Fig. 6), the difference between WRF and ROMS/CICE in surface sensible and latent heat fluxes is negligible (mostly less than 0.1 W/m^2) throughout the simulation of Exp_FREE. In contrast, the inconsistency in surface turbulent heat fluxes is more pronounced in Exp_FREE_OLD (Fig. 6). The differences in sensible heat flux are mostly positive throughout the simulation, with the magnitude of differences ranging from ~2.5 to ~12.5 W/m^2 (Fig. 6c). The differences in latent heat flux are mostly positive from September 2019 to April 2020 (up to 7.5 W/m^2) and then negative afterward (up to 7.5 W/m^2) (Fig. 6d). The combined effects of the inconsistency in surface heat flux budget are 0~15 W/m^2 for most of the simulation period in Exp_FREE_OLD (Fig. S4 in the supplement). In this study, all fluxes are defined as positive downward. Hence, positive (negative) inconsistency in surface heat flux budget represents that ROMS/CICE uses less (more) energy than it supposes to be as the top boundary condition to update state variables in ROMS/CICE, which can be also viewed as an artificial cooling (warming) effect in the ocean-sea ice coupled system due to the surface heat flux inconsistency.

To further illustrate how the inconsistency in surface heat fluxes degrades the performance of CAPS with the original coupling approach (in Exp_FREE_OLD), the evolutions of sea ice volume (SIV) budget components (with their terminology according to Appendix E of Notz et al., 2016) for Exp_FREE and Exp_FREE_OLD are compared (Figure 7). Overall, the total SIV tendencies in Exp_FREE_OLD (Fig. 7a) are higher than those in Exp_FREE (Fig. 7a) for most of the simulation, with largest differences (up to 0.2 cm/day) between both experiments in July 2020 compared to the rest of the simulation. The higher total SIV tendencies in

https://doi.org/10.5194/egusphere-2026-362
Preprint. Discussion started: 10 March 2026

Exp_FREE_OLD indicates that the simulated SIT in Exp_FREE_OLD will become thicker than that in Exp_FREE as the model integrates, which is also shown in the average SIT in March and September 2020 (Fig. S2). The thicker SIT contributes slower retreating of sea ice coverage during the melting season in Exp_FREE_OLD, corresponding to significantly overestimated SIE shown in Figure 3a. Compared to Exp_FREE, Exp_FREE_OLD shows higher SIV growth rate at the bottom of the ice (basal growth, Fig. 7f) and from supercooled open water (frazil, Fig. 7g) in 2019/2020 winter and spring, and significantly less SIV melting at the atmosphere–ice interface (top melt, Fig. 7b) in summer 2020. Figure 8 shows the heat flux budget components at the atmosphere–ice interface and the ice–ocean interface for both Exp_FREE and Exp_FREE_OLD. Generally, the net heat flux at the atmosphere–ice interface (Fig. 8a) is well correlated to the total SIV tendencies shown in Figure 7a. Larger negative net heat fluxes (i.e., sea ice loses energy to the atmosphere) contribute to larger SIV growth. Accordingly, the larger negative heat flux in Exp_FREE_OLD compared to Exp_FREE drives the larger SIV growth in Exp_FREE_OLD in winter, particularly in January 2020. And, the smaller positive net heat fluxes (i.e., sea ice gains energy from the atmosphere) in Exp_FREE_OLD, compared to Exp_FREE, in July 2020 are responsible for the smaller SIV melting in Exp_FREE_OLD. The decomposition of the net heat fluxes at the ice surface to radiative and turbulent components (Figs. 8b-d) shows that the larger negative net heat fluxes from October 2019 to December 2019 in Exp_FREE_OLD are caused by the combination of latent heat flux and net longwave radiation loss at the surface (which are partially cancelled by oscillated positive sensible heat fluxes). The smaller positive net heat fluxes in

https://doi.org/10.5194/egusphere-2026-362
Preprint. Discussion started: 10 March 2026

Exp_FREE_OLD in July 2020 are mainly dominated by smaller net shortwave radiative fluxes. In contrast to net heat fluxes at the atmosphere–ice interface, net heat fluxes at the ice–ocean interface does not show clear contributions to SIV tendencies in Exp_FREE_OLD (Fig. 7, 8f).

3.2 Evaluation based on the MOSAiC observations

3.2.1. Snow and ice mass balance

The evolutions of SIT and snow depth for the observations and the simulations along the MOSAiC drift are shown in Figure 9. For SIT (Fig. 9, lower box), SIMBA shows ~1.0 m ice thickness at the beginning of December 2019 and reaches ~1.9 m at the beginning of June 2020. The simulated SIT of Exp_FREE and Exp_NUD show some disagreement with that of the SIMBA buoys, which is partly associated with that the simulations do not reproduce exactly the same ice trajectory as the track of SIMBA buoys. Exp_FREE shows similar SIT as the SIMBA buoys at the beginning of December 2019 and comparable thickening changes from December 2019 to February 2020. Afterwards, SIT in Exp_FREE shows early thinning changes relative to the SIMBA buoys. On the other hand, SIT in Exp_NUD shows overall thickening evolutions, which are relatively similar to those by the SIMBA buoys. Exp_NUD also shows thicker SIT compared to the SIMBA buoys (~1.2 m vs. ~1.0 m, which still lies within the uncertainty range of SIMBA) at the beginning of December 2019. For snow depth (Fig. 9, upper box), snow depth observed by the SIMBA buoys is near constant (~20 cm) from December 2019 to June 2020 and then decreases afterward. Both Exp_FREE and Exp_NUD can simulate the timing of snow depth decreases. However, they also show a throughout snow depth thickening in contrast to near constant snow depth shown in the observations from

https://doi.org/10.5194/egusphere-2026-362
Preprint. Discussion started: 10 March 2026

December 2019 to May 2020. Also, Exp_NUD shows relatively larger snow accumulation than Exp_FREE.

Similar to SIV budget averaged for the entire domain discussed in Section 3.1, the snow and sea ice volume budgets along the track of SIMBA buoys for Exp_FREE and Exp_NUD are shown in Figure 10 to interpret the above-described simulated biases. The figure indicates that the evolutions of SIT (shown in Fig. 9), especially the SIT thinning, are primarily driven by basal melt for both Exp_FREE and Exp_NUD. Exp_FREE shows larger basal melt and earlier increases in basal melt than Exp_NUD. For snow depth, the thickening of snow depth in Exp_FREE and Exp_NUD are associated with individual snowing events (i.e., spikes in snow fall shown in Fig. 10a, upper box). Since snow volume budgets in Exp_FREE and Exp_NUD are well correlated with the evolutions of snow depth shown in Figure 9, this indicates that the discrepancy between the simulated snow depth and the SIMBA observations may be associated with missing processes in the CICE model. Currently, ice thermodynamics in the CICE model (Bitz and Lipscomb, 1999; Turner and Hunke, 2015) treat snow and ice as an integral, and snow is not independently transported to other grid cells by surface wind.

3.2.2. Surface atmospheric energy budget

Figure 11 shows radiative and turbulent heat fluxes at the ice surface for the observations and the simulations along the MOSAiC drift. For net shortwave radiative flux (NetSW, Fig. 11a), Exp_FREE, Exp_NUD, and the observations show similar evolution of NetSW from March to June 2020. Afterward, both Exp_FREE and Exp_NUD simulate smaller peak of NetSW in mid-June 2020 with underestimations of ~40 W/m^2 for both Exp_FREE and

https://doi.org/10.5194/egusphere-2026-362
Preprint. Discussion started: 10 March 2026

Exp_NUD compared with the observations. For net longwave radiative flux (NetLW, Fig. 11b), Exp_FREE and Exp_NUD, show different periods with smaller biases compared with the observations from November 2019 to June 2020. Afterward, both Exp_FREE and Exp_NUD show overestimations (~15-25 W/m^2 for Exp_FREE, ~10-15 W/m^2 for Exp_NUD) of NetLW compared to the observed values. For turbulent heat fluxes (Fig. 11c-d), both Exp_FREE and Exp_NUD show similar evolution of sensible and latent heat fluxes (SH and LH), and the simulated SH and LH are similar to the observations from November 2019 to February 2020. Afterward, the simulated SH and LH begin to show biases compared with the observed SH and LH, especially the simulated LH from May 2020 to June 2020. Both Exp_FREE and Exp_NUD show different timings with smaller/larger biases in NetLW, SH, and LH compared to the observed values, indicating the grid cell nearest to the locations of the observations in Exp_FREE and Exp_NUD are experiencing different synoptic systems in the atmosphere during the simulation period. Although Exp_FREE and Exp_NUD show biases in net radiative and turbulent heat fluxes, the net heat fluxes over the ice surface, which is the major factor determining changes in ice temperature, ice melt, and ice growth in CICE, show better agreement with the observational values for both Exp_FREE and Exp_NUD due to bias cancellation (Fig. S5 in the supplement).

3.2.3. Atmospheric profile

Figure 12 shows the vertical profiles of atmosphere temperature and relative humidity (RH) measured by radiosondes launched during the MOSAiC expedition, and the difference between the observations and the experiments along the track of MOSAiC drift. For

https://doi.org/10.5194/egusphere-2026-362
Preprint. Discussion started: 10 March 2026

atmospheric temperature profiles, Exp_FREE simulates profiles with biases oscillating between warm and cold, and the magnitude of biases is larger from October 2019 to April 2020 (Fig. 12b) compared to the rest of periods. From December 2019 to April 2020, Exp_FREE shows excessively warm biases (over 10 degrees Celsius) above ~8km altitude. In contrast to Exp_FREE, the simulated temperature profiles in Exp_NUD show much better agreement with the observed profiles (Fig. 12c). For RH profiles, Exp_FREE simulates mainly dryer profiles with intermittent wetter profiles relative to the radiosondes (Fig. 12e). These intermittent profiles are mainly wetter above ~500 m altitude. Below ~500 m altitude, these intermittent profiles are generally dryer compared to the radiosondes. Exp_NUD shows similar patterns in RH profiles (i.e., generally dryer, and intermittently wetter above ~500 m altitude) as Exp_FREE, but smaller differences relative to the observations (Fig. 12f). The differences in temperature and RH profiles between Exp_FREE and Exp_NUD shown in Figure 12b-c are partly associated with the simulated synoptic systems compared with the observations. MOSAiC was characterized by anomalous high frequencies of storms relative to the period of 1979-2020 impacting the trajectory of MOSAiC drift (Liang et al., 2025). These storm events were associated with anomalous meteorological conditions during the MOSAiC period such as anomalously warm conditions by storms during 16th to 20th November 2019, and anomalously low sea level pressure condition by storms during 11th to 25th March 2020 (hereafter referred as STORM-1 and STORM-2; Rinke et al., 2021). The average mean sea level pressure (MSLP), near-surface air temperature (T2), and 10 m wind fields (UV10) in ERA5, Exp_FREE, and Exp_NUD for the period of STORM-1 and STORM-2 are shown in Figure 13. The average

https://doi.org/10.5194/egusphere-2026-362
Preprint. Discussion started: 10 March 2026

temperature and RH profiles for Exp_FREE, Exp_NUD, and the radiosondes are also shown in the supplement (Fig. S6) during both storm periods. During the STORM-1 period, in ERA5, the averaged location of radiosondes (Fig. 13, white stars) is positioned in the central Arctic encompassing by a low-pressure system (Fig. 13a). Exp_FREE also simulates a low-pressure system with lower MSLP encompassing the averaged location of radiosondes (Fig. 13b). The similarity of atmospheric circulations between ERA5 and Exp_FREE near the averaged location of radiosondes results in similar average temperature profiles from surface to 7 km altitude (Fig. S6). During the STORM-2 period, a low-pressure system located at the Barents-Kara Seas encompasses the radiosondes in ERA5 (Fig. 13d) while Exp_FREE shows a low-pressure system centered at the Greenland Sea and the averaged location of radiosondes is positioned at the location with higher MSLP (Fig. 13e). The atmospheric circulations and temperature fields in Exp_FREE result in the warm advection from the North Atlantic to the location of MOSAiC during the STORM-2 period (Fig. 13k), which is partly contributed to the warmer profiles in Exp_FREE from surface to ~7 km altitude (Fig. 12 and Fig. S6b). Exp_FREE also shows enhanced warm biases above ~7 km altitude for both STORM-1 and STORM-2 period (Fig. S6a-b). With the temperature and wind fields at 8 to 10 km altitude (Fig. S7 in the supplement), it shows that the warm bias in Exp_FREE increases with altitude and the bias pattern is near barotropic. This may be associated with biases from the stratosphere and the model top boundary as suggested by Cassano et al. (2011). In contrast to Exp_FREE, the simulated atmospheric circulations and temperature fields in Exp_NUD resemble those in ERA5 during both storm periods (Fig. 13) corresponding to small temperature biases shown in

https://doi.org/10.5194/egusphere-2026-362
Preprint. Discussion started: 10 March 2026

the simulated profiles (Fig. 12c, Fig. S6a-b). Exp_NUD, which applies the nudging scheme to the upper levels, can well reproduce the atmospheric circulations and temperature fields for other periods during MOSAiC (not shown). However, CAPS with the nudging scheme still faces challenges in simulating RH conditions during the STORM-1 and STORM-2 periods (Fig. S6c-d). As shown by Figures 12 and 13, the accuracy in simulating the synoptic conditions is crucial for CAPS reproducing the observed vertical thermal structure in the Arctic. The results show that larger biases in Exp_FREE from December 2019 to April 2020 described above (Fig. 12) are partly associated with that Exp_FREE does not properly reproduce these synoptic systems during this period. Liang et al. (2025) also shows that the storm events impacting the MOSAiC site are mostly concentrated in the ice growth period (November 2019 to March 2020).

3.2.4. Ocean profile

Figure 14 shows the vertical profiles of ocean temperature and salinity in the upper 100 m observed by CTD buoys, and the difference between the observations and the simulations along the MOSAiC drift. Unlike the comparisons with sea ice and atmospheric measurements described above, Exp_FREE and Exp_NUD show similar patterns of simulated ocean temperature and salinity in upper ocean layer before mid-June 2020.

For oceanic temperature profiles (Fig. 14b-c), both experiments show slightly warmer temperatures (less than 0.1 degree Celsius) in the upper 30 m before July 2020 than the observational values. Before February 2020, both experiments show slightly warmer temperatures (differences of 0.2~0.4 degrees Celsius) between 30 m to 80 m layer. From March

https://doi.org/10.5194/egusphere-2026-362
Preprint. Discussion started: 10 March 2026

2020 to June 2020, the positive differences increase with depth such that the experiments simulate 0.5~1.0 degrees Celsius warmer ocean temperatures in 60 m to 100 m layers. Both experiments also show slightly colder temperatures between 80 m to 100 m layer before January 2020. Overall, the simulated oceanic temperature in Exp_NUD shows slightly better agreement with the CTD data than that in Exp_FREE. For salinity profiles (Fig. 14e-f), both experiments show fresher (1.0~2.0 psu) upper layer before December 2019. Afterward, both experiments begin to show better agreement (-0.25~0.25 psu differences) with the observed salinity in the upper 40 m, and then the depth with agreement extends to 100 m until May 2020. Similar to oceanic temperature profiles, Exp_NUD also shows slightly better agreement with the observed salinity profiles than Exp_FREE.

After June 2020, the significant differences in oceanic temperature and salinity between the simulations and observations are associated with the simulated SIC and the upper ocean thermal structure along the track of CTD buoys. Both Exp_FREE and Exp_NUD show warm biases around July 2020 for the 10-100 m layer and warm biases in Exp_FREE (over 1.5 degrees) are much larger than those in Exp_NUD (~0.5 degrees). These warm biases in Exp_FREE and Exp_NUD correspond to SIC less than 0.9 while the observations still show near 1.0 SIC as shown in Figure S8 in the supplement. The spatial distribution of temperature and salinity of Exp_FREE and Exp_NUD at 10, 50, and 100 m depth on July 1st, 2020, also indicates that the biases shown in Figure 14 are associated with the simulated Atlantic inflows (Fig. S9 in the supplement).

4. Conclusions and Discussions

https://doi.org/10.5194/egusphere-2026-362
Preprint. Discussion started: 10 March 2026

This study introduces an improved version of Coupled Arctic Prediction System (CAPS) that conserves surface heat fluxes between the atmosphere and ocean components of CAPS. A set of pan-Arctic numerical experiments covering the entire MOSAiC expedition have been carried out for demonstrating the improvement in simulating Arctic sea ice conditions from the conservation of surface heat fluxes, and for the evaluation of improved CAPS in simulating Arctic climate system based on the MOSAiC observations.

The results show that the inconsistency in surface heat fluxes shown in the previous version of CAPS has been significantly minimized with the revised coupling approach, and the simulated Arctic sea ice conditions with the improved CAPS are more comparable to satellite-based sea ice observations than those with the previous version of CAPS. The model evaluation against the MOSAiC observations demonstrates that CAPS, with applying the spectral nudging applied to the upper model levels in the atmosphere component, can better reproduce the atmospheric, oceanic, and sea ice conditions compared to the observations along the track of MOSAiC expedition than its counterpart without utilizing the spectral nudging technique. In this study, the simulated sea ice conditions are sensitive to the choices of physics options in both the atmospheric and ice-ocean model components used in the free simulation (Exp_FREE). Simulations conducted with the improved CAPS choosing the same physics options used in the previous version of CAPS (e.g., Yang et al., 2022) can result in the underperformance of the simulated sea ice conditions (not shown). This indicates further investigations of physical processes in CAPS are required to further improve the performance of CAPS. Firstly, CAPS faces challenges to simulate surface heat flux budget over the ice surface regardless with or

https://doi.org/10.5194/egusphere-2026-362
Preprint. Discussion started: 10 March 2026

582 without the spectral nudging. Liu et al. (2024) found that the atmospheric boundary layer
583 observed during MOSAiC can be categorized into a surface inversion type and an elevated
584 inversion type, and the enhanced non-local effects associated with a surface inversion type pose
585 difficulties on similarity theory-based parametrizations to simulate surface sensible heat fluxes.
586 Secondly, CAPS does not well reproduce the timings and the height of temperature inversions
587 compared with the radiosonde, in particular the simulation without applying spectral nudging
588 (Exp_FREE), throughout the MOSAiC period as shown in Figure S10 in the supplement. The
589 strong temperature inversions in wintertime Arctic have important effects on the magnitude of
590 downward longwave radiation near the surface (Bintanja et al., 2011). The simulated downward
591 longwave radiation is shown to be associated with the boundary layer stability (e.g., Jozef et
592 al., 2024). Thirdly, surface radiative heat fluxes are regulated by clouds (e.g., Curry et al., 1996;
593 e.g., Shupe and Intrieri, 2004). However, it is still challenging for CAPS to properly reproduce
594 liquid water content (LWC) and ice water content (IWC) associated with the frequent
595 occurrence of Arctic mixed-phase clouds and their associated radiative impacts (e.g., Tan et al.,
596 2023) during the MOSAiC expedition. Here, an additional experiment is conducted for the
597 STORM-1 period with high-frequency outputs for cloud properties, and the calculated LWC
598 and IWC compared with the MOSAiC observations are shown in Figure 15. Generally, CAPS
599 strongly underestimates both LWC and IWC during the STORM-1 period in terms of the
600 occurrence and the vertical distribution, which corresponds to the simulated dryer atmospheric
601 profiles (Fig. 12). The underestimations of LWC and IWC are associated with the treatment in
602 the microphysics and the atmospheric boundary layer schemes (e.g., Arteaga et al., 2024;

https://doi.org/10.5194/egusphere-2026-362
Preprint. Discussion started: 10 March 2026

Sedlar et al., 2020). Arteaga et al. (2024) also suggest that increases in the cloud condensation nuclei and droplet number concentrations in the microphysics schemes can have impacts on the simulated LWC and IWC. Furthermore, it is essential to increase model resolution both horizontally and vertically to properly simulate the phase heterogeneity in Arctic clouds (e.g., Dammann et al., 2025), which demands more computational resources for high-resolution simulations.

Regardless of the challenges posed to CAPS, the conservation of surface heat fluxes exchange between the atmosphere and the ocean in CAPS provides a solid foundation for future improvements of representation of physical processes, especially for processes related to surface heat flux calculations. Additionally, the simulated sea ice conditions are less sensitive to different combinations of physical options when the spectral nudging is applied in the atmosphere component of CAPS, and our results also show that the nudging experiment can reproduce similar atmospheric circulations compared with ERA5 (Fig. 13). This indicates CAPS is potentially applicable to the storyline approaches (e.g., Baldissera Pacchetti et al., 2024), that investigate how past events, for example, “Great Arctic Cyclone” of 2012 (Simmonds and Rudeva, 2012), influence sea ice changes under different climate scenarios.

In this study, the implementation of our revised coupling approach is based on the shared horizontal grid between the atmosphere component and the ocean-sea ice component. For applications that require higher resolution (e.g., sea ice linear kinematic features, ocean eddies in polar oceans), both the atmosphere model and the ocean-sea ice model have to increase their resolutions to the same grid in our current coupling approach, which may be computationally

https://doi.org/10.5194/egusphere-2026-362
Preprint. Discussion started: 10 March 2026

unrealistic for the atmosphere component. CAPS does have the capability for the atmosphere component and the ocean-sea ice component using different grids through the interpolation weightings generated by the Earth System Modeling Framework (ESMF). However, the interpolation is mask-to-mask basis in CAPS, i.e., a smaller ocean-sea ice grid cell may represent a larger ocean mask (especially near the complex topography) in the atmosphere component. That is, the spatial heterogeneity of the surface types (i.e., the mixture of land, ocean, and sea ice) within a larger atmosphere grid cell is not properly treated. This will lead to less flux consistency between the atmosphere component and the ocean-sea ice component. Recently, a regional modeling system developed by Karsten et al. (2024), which applies a flux coupling approach (e.g., Balaji et al., 2006) on an exchange grid, demonstrates the future direction of improving our coupling approach for wider applications. With the flux coupling approach on an exchange grid, a locally consistent treatment of the surface fluxes between model components with independent grids is achievable.

https://doi.org/10.5194/egusphere-2026-362
Preprint. Discussion started: 10 March 2026

Code and data availability:

This study uses publicly available sea-ice satellite observations, atmosphere, and ocean reanalysis from the original data providers: NSIDC-0051 sea-ice concentration (https://nsidc.org/data/nsidc-0051/versions/2; last access: 30 Nov 2025), CS2SMOS sea-ice thickness (https://data.meereisportal.de/relaunch/CS2SMOS.php; last access: 30 Nov 2025), PIOMAS sea-ice thickness (https://psc.apl.uw.edu/research/projects/arctic-sea-ice-volume-anomaly/data/; last access: 30 Nov 2025), ERA5 atmospheric reanalysis (https://cds.climate.copernicus.eu/datasets/; last access: 30 Nov 2025), and CMEMS GREP ocean and sea-ice products (https://data.marine.copernicus.eu/products; last access: 30 Nov 2025). MOSAiC datasets were obtained from the following DOIs: radiosonde data (Maturilli et al., 2022; https://doi.pangaea.de/10.1594/PANGAEA.943870), cloud microphysics (Shupe, 2022; https://doi.org/10.5439/1871015), surface fluxes (Cox et al., 2023a–d; https://doi.org/10.18739/A2PV6B83F; https://doi.org/10.18739/A2FF3M18K; https://doi.org/10.18739/A25X25F0P; https://doi.org/10.18739/A2XD0R00S), CTD data (Hoppmann et al., 2022; https://doi.pangaea.de/10.1594/PANGAEA.940271), and SIMBA data (Lei et al., 2021; https://doi.org/10.1594/PANGAEA.938267).

To ensure full and long-term reproducibility, the exact evaluation datasets used in this study (including NSIDC-0051, CS2SMOS, PIOMAS sea ice data, and the processed MOSAiC datasets used for evaluation) are archived in Zenodo repository: https://doi.org/10.5281/zenodo.18764432 (Yang, 2026a). The exact model version used to produce the results is archived in Zenodo repository: https://doi.org/10.5281/zenodo.18308943 (Yang, 2026b). The pan-Arctic simulation outputs analyzed in this study are archived in Zenodo repository: https://doi.org/10.5281/zenodo.18308549 (Yang, 2026c).

Author contributions: CYY implemented the revised coupling approach in CAPS,

https://doi.org/10.5194/egusphere-2026-362
Preprint. Discussion started: 10 March 2026

conducted numerical experiments, and wrote the original manuscript. FG performed the evaluation based on the MOSAiC data. CYY and JL were responsible for the conceptualization of this study. CYY, FG, JL, and AR were responsible for the revisions of the manuscript. All co-authors reviewed and commented on the final version of the manuscript.

Competing interests: The authors declare that they have no conflict of interest.

Acknowledgements: This research is supported by the National Natural Science Foundation of China (42376237), and the Innovation Group Project of Southern Marine Science and Engineering Guangdong Laboratory (Zhuhai) (311021008).

https://doi.org/10.5194/egusphere-2026-362
Preprint. Discussion started: 10 March 2026

5. References

Arteaga, D., Planche, C., Tridon, F., Dupuy, R., Baudoux, A., Banson, S., Baray, J.-L., Mioche, G., Ehrlich, A., Mech, M., Mertes, S., Wendisch, M., Wobrock, W., and Jourdan, O.: Arctic mixed-phase clouds simulated by the WRF model: Comparisons with ACLOUD radar and in situ airborne observations and sensitivity of microphysics properties, Atmos. Res., 307, 107471, https://doi.org/10.1016/j.atmosres.2024.107471, 2024.

Balaji, V., Anderson, J., Held, I., Winton, M., Durachta, J., Malyshev, S., and Stouffer, R. J.: The Exchange Grid: a mechanism for data exchange between Earth System components on independent grids, in: Parallel computational fluid dynamics 2005, 179–186, Elsevier, https://doi.org/10.1016/B978-044452206-1/50021-5, 2006.

Baldissera Pacchetti, M., Coulter, L., Dessai, S., Shepherd, T. G., Sillmann, J., and Van Den Hurk, B.: Varieties of approaches to constructing physical climate storylines: A review. WIREs Climate Change, 15(2), e869. https://doi.org/10.1002/wcc.869, 2024.

Bintanja, R., Graversen, R. and Hazeleger, W.: Arctic winter warming amplified by the thermal inversion and consequent low infrared cooling to space. Nature Geosci., 4, 758–761, https://doi.org/10.1038/ngeo1285, 2011.

Bitz, C. M. and Lipscomb, W. H.: An energy-conserving thermodynamic sea ice model for climate study. J. Geophys. Res.-Oceans, 104, 15669–15677, https://doi.org/10.1029/1999JC900100, 1999.

Bliss, A. C., Hutchings, J. K., and Watkins, D. M.: Sea ice drift tracks from autonomous buoys in the MOSAiC Distributed Network, Scientific Data, 10, 403, https://doi.org/10.1038/s41597-023-02311-y, 2023.

Briegleb, B. P. and Light, B.: A Delta-Eddington multiple scattering parameterization for solar radiation in the sea ice component of the Community Climate System Model. (No. NCAR/TN-472+STR). University Corporation for Atmospheric Research, https://doi.org/10.5065/D6B27S71, 2007.

https://doi.org/10.5194/egusphere-2026-362
Preprint. Discussion started: 10 March 2026

Cassano, J. J., Higgins, M. E., and Seefeldt, M. W.: Performance of the Weather Research and Forecasting Model for Month-Long Pan-Arctic Simulations. Monthly Weather Review, 139, 11, 3469-3488, https://doi.org/10.1175/MWR-D-10-05065.1, 2011.

Chen, F. and Dudhia, J.: Coupling an advanced land surface–hydrology model with the Penn State–NCAR MM5 modeling system. Part I: Model implementation and sensitivity. Mon. Wea. Rev., 129, 569–585, https://doi.org/10.1175/1520-0493(2001)129<0569:CAALSH>2.0.CO;2, 2001.

Cocetta, F., Zampieri, L., Selivanova, J., and Iovino, D.: Assessing the representation of Arctic sea ice and the marginal ice zone in ocean–sea ice reanalyses, The Cryosphere, 18, 4687–4702, https://doi.org/10.5194/tc-18-4687-2024, 2024.

Cohen, J., Screen, J. A., Furtado, J. C., Barlow, M., Whittleston, D., Coumou, D., Francis, J., Dethloff, K., Entekhabi, D., Overland, J., and Jones, J.: Recent Arctic amplification and extreme mid-latitude weather. Nature Geosci 7, 627–637, https://doi.org/10.1038/ngeo2234, 2014.

Cohen, J., Zhang, X., Francis, J., Jung, T., Kwok, R., Overland, J., Ballinger, T. J., Bhatt, U. S., Chen, H. W., Coumou, D., Feldstein, S., Gu, H., Handorf, D., Henderson, G., Ionita, M., Kretschmer, M., Laliberte, F., Lee. S, Linderholm, H. W., Maslowski, W., Peings, Y., Pfeiffer, K., Rigor, I., Semmler, T., Stroeve, J., Taylor, P. C., Vavrus, S., Vihma, T., Wang, S., Wendisch, M., Wu, Y., and Yoon, J.: Divergent consensuses on Arctic amplification influence on midlatitude severe winter weather. Nat. Clim. Chang. 10, 20–29, https://doi.org/10.1038/s41558-019-0662-y, 2020.

Cox, C. J., Gallagher, M., Shupe, M., Persson, O., Blomquist, B., Grachev, A., Riihimaki, L., Kutchenreiter, M., Morris, V., Solomon, A., Brooks, I., Costa, D., Gottas, D., Hutchings, J., Osborn, J., Morris, S., Preusser, A., and Uttal, T.: Met City meteorological and surface flux measurements (Level 3 Final), Multidisciplinary Drifting Observatory for the Study of Arctic Climate (MOSAiC), central Arctic, October 2019 – September 2020. *Arctic Data Center* [data set], https://doi.org/10.18739/A2PV6B83F, 2023a.

https://doi.org/10.5194/egusphere-2026-362
Preprint. Discussion started: 10 March 2026

727 Cox, C. J., Gallagher, M., Shupe, M., Persson, O., Blomquist, B., Grachev, A., Riihimaki, L.,
728 Kutchenreiter, M., Morris, V., Solomon, A., Brooks, I., Costa, D., Gottas, D., Hutchings,
729 J., Osborn, J., Morris, S., Preusser, A., and Uttal, T.: Atmospheric Surface Flux Station
730 #30 measurements (Level 3 Final), Multidisciplinary Drifting Observatory for the Study
731 of Arctic Climate (MOSAiC), central Arctic, October 2019 – September 2020. Arctic Data
732 Center [data set], https://doi.org/10.18739/A2FF3M18K, 2023b.
733 Cox, C. J., Gallagher, M., Shupe, M., Persson, O., Blomquist, B., Grachev, A., Riihimaki, L.,
734 Kutchenreiter, M., Morris, V., Solomon, A., Brooks, I., Costa, D., Gottas, D., Hutchings,
735 J., Osborn, J., Morris, S., Preusser, A., and Uttal, T.: Atmospheric Surface Flux Station
736 #40 measurements (Level 3 Final), Multidisciplinary Drifting Observatory for the Study
737 of Arctic Climate (MOSAiC), central Arctic, October 2019 – September 2020. Arctic Data
738 Center [data set], https://doi.org/10.18739/A25X25F0P, 2023c.
739 Cox, C. J., Gallagher, M., Shupe, M., Persson, O., Blomquist, B., Grachev, A., Riihimaki, L.,
740 Kutchenreiter, M., Morris, V., Solomon, A., Brooks, I., Costa, D., Gottas, D., Hutchings,
741 J., Osborn, J., Morris, S., Preusser, A., and Uttal, T.: Atmospheric Surface Flux Station
742 #50 measurements (Level 3 Final), Multidisciplinary Drifting Observatory for the Study
743 of Arctic Climate (MOSAiC), central Arctic, October 2019 – September 2020. Arctic Data
744 Center [data set], https://doi.org/10.18739/A2XD0R00S, 2023d.
745 Curry, J. A., Schramm, J. L., Rossow, W. B., and Randall, D.: Overview of Arctic Cloud and
746 Radiation Characteristics, J. Climate, 9, 1731–1764, https://doi.org/10.1175/1520-
747 0442(1996)009<1731:OOACAR>2.0.CO;2, 1996.
748 Dammann, S. L.-S., Schäfer, B., David, R. O., and Storelvmo, T.: Observations and model
749 simulations of phase heterogeneity in Arctic clouds. Journal of Geophysical Research:
750 Atmospheres, 130, e2024JD042714. https://doi.org/10.1029/2024JD042714, 2025.
751 Deng, J., and Dai, A.: Sea ice–air interactions amplify multidecadal variability in the North
752 Atlantic and Arctic region. Nat Commun 13, 2100, https://doi.org/10.1038/s41467-022-
753 29810-7, 2022.

https://doi.org/10.5194/egusphere-2026-362
Preprint. Discussion started: 10 March 2026

754 Deng, J., and Dai, A.: Arctic sea ice–air interactions weaken El Niño–Southern Oscillation. Sci.
755 Adv., 10, eadk3990, https://doi.org/10.1126/sciadv.adk3990, 2024
756 DiGirolamo, N. E., Parkinson, C. L., Cavalieri, D. J., Gloersen, P., and Zwally, H. J.: updated
757 yearly. Sea Ice Concentrations from Nimbus-7 SMMR and DMSP SSM/I-SSMIS Passive
758 Microwave Data, Version 2. Boulder, Colorado USA, NASA National Snow and Ice Data
759 Center Distributed Active Archive Center [data set],
760 https://doi.org/10.5067/MPYG15WAA4WX, 2022.
761 Durski, S. M., Glenn, S. M., and Haidvogel, D. B.: Vertical mixing schemes in the coastal
762 ocean: Comparison of the level 2.5 Mellor-Yamada scheme with an enhanced version of
763 the K profile parameterization, J. Geophys. Res., 109, C01015,
764 https://doi.org/10.1029/2002JC001702, 2004.
765 Fairall, C. W., Bradley, E. F., Hare, J. E., Grachev, A. A., and Edson, J. B.: Bulk
766 Parameterization of Air–Sea Fluxes: Updates and Verification for the COARE Algorithm.
767 Journal of Climate, 16(4), 571-591. https://doi.org/10.1175/1520-
768 0442(2003)016<0571:BPOASF>2.0.CO;2, 2003.
769 Freitas, S. R., Grell, G. A., Molod, A., Thompson, M. A., Putman, W. M., Santos e Silva, C.
770 M. and Souza, E. P.: Assessing the Grell–Freitas convection parameterization in the
771 NASA GEOS modeling system. J. Adv. Model. Earth Syst., 10, 1266–1289,
772 https://doi.org/10.1029/2017MS001251, 2018.
773 Giles, K. A, Laxon, S. W., Ridout, A. L., Wingham, D. J., and Bacon, S.: Western Arctic Ocean
774 freshwater storage increased by wind-driven spin-up of the Beaufort Gyre. Nat. Geosci.
775 5, 194–197, https://doi.org/10.1038/ngeo1379, 2012.
776 Goessling, H. F., Tietsche, S., Day, J. J., Hawkins, E., and Jung, T.: Predictability of the Arctic
777 sea ice edge, Geophys. Res. Lett., 43, 1642–1650, https://doi.org/10.1002/2015GL067232,
778 2016.
779 Gutowski Jr., W. J., Giorgi, F., Timbal, B., Frigon, A., Jacob, D., Kang, H.-S., Raghavan, K.,
780 Lee, B., Lennard, C., Nikulin, G., O'Rourke, E., Rixen, M., Solman, S., Stephenson, T.,

https://doi.org/10.5194/egusphere-2026-362
Preprint. Discussion started: 10 March 2026

781 and Tangang, F.: WCRP COordinated Regional Downscaling EXperiment (CORDEX): a
782 diagnostic MIP for CMIP6, Geosci. Model Dev., 9, 4087–4095,
783 https://doi.org/10.5194/gmd-9-4087-2016, 2016.
784 Haas, C.: Sea ice thickness distribution, In Sea Ice, D.N. Thomas (Ed.).
785 https://doi.org/10.1002/9781118778371.ch2, 2017.
786 Hersbach, H., Bell, B., Berrisford, P., Biavati, G., Horányi, A., Muñoz Sabater, J., Nicolas, J.,
787 Peubey, C., Radu, R., Rozum, I., Schepers, D., Simmons, A., Soci, C., Dee, D., Thépaut,
788 J-N.: ERA5 hourly data on single levels from 1940 to present, Copernicus Climate Change
789 Service (C3S) Climate Data Store (CDS) [data set],
790 https://doi.org/10.24381/cds.adbb2d47, 2023.
791 Holland, M.M., and Bitz, C. M.: Polar amplification of climate change in coupled models.
792 Climate Dynamics 21, 221–232, https://doi.org/10.1007/s00382-003-0332-6, 2003.
793 Hoppmann, M., Kuznetsov, I., Fang, Y.-C., Rabe, B.: Processed data of CTD buoys 2019O1 to
794 2019O8 as part of the MOSAiC Distributed Network, PANGAEA [data set],
795 https://doi.org/10.1594/PANGAEA.940320, 2022.
796 Hunke, E. C. and Dukowicz, J. K.: An elastic-viscous-plastic model for sea ice dynamics. J.
797 Phys. Oceanogr. 27, 1849–67, https://doi.org/10.1175/1520-
798 0485(1997)027<1849:AEVPMF>2.0.CO;2, 1997.
799 Hunke, E. C., Hebert, D. A., and Lecomte, O.: Level-ice melt ponds in the Los Alamos Sea Ice
800 Model, CICE. Ocean Modelling, 71, 26–42,
801 https://doi.org/10.1016/j.ocemod.2012.11.008, 2013.
802 Huntemann, M., Heygster, G., Kaleschke, L., Krumpen, T., Makynen, M., and Drusch, M.:
803 Empirical sea ice thickness retrieval during the freeze-up period from SMOS high incident
804 angle observations, Cryosphere, 8, 439–451, https://doi.org/10.5194/tc-8-439-2014, 2014.
805 Iacono, M. J., Delamere, J. S., Mlawer, E. J., Shephard, M. W., Clough, S. A., and Collins, W.
806 D.: Radiative forcing by long-lived greenhouse gases: Calculations with the AER radiative

https://doi.org/10.5194/egusphere-2026-362
Preprint. Discussion started: 10 March 2026

807 transfer models, J. Geophys. Res., 113, D13103, https://doi.org/10.1029/2008JD009944,
808 2008.
809 Irving, D., Hobbs, W., Church, J., and Zika, J.: A Mass and Energy Conservation Analysis of
810 Drift in the CMIP6 Ensemble. *Journal of Climate*, *34*(8), 3157-
811 3170. https://doi.org/10.1175/JCLI-D-20-0281.1, 2021.
812 Jordan, R. E., Andreas, E. L., and Makshtas, A. P.: Heat budget of snow-covered sea ice at
813 North Pole 4, J. Geophys. Res.-Oceans, 104(C4), 7785–7806,
814 http://doi.org/10.1029/1999JC900011, 1999.
815 Jozef, G., Cassano, J. J., Solomon, A., Intrieri, J., Boer, G.: Evaluation of the Coupled Arctic
816 Forecast System's representation of the Arctic atmospheric boundary layer vertical
817 structure during MOSAiC. Elementa: Science of the Anthropocene, 12 (1): 00136,
818 https://doi.org/10.1525/elementa.2023.00136, 2024.
819 Kacimi, S. and Kwok, R.: Two Decades of Arctic Sea-Ice Thickness from Satellite Altimeters:
820 Retrieval Approaches and Record of Changes (2003–2023). Remote Sens., 16, 2983.
821 https://doi.org/10.3390/rs16162983, 2024.
822 Karsten, S., Radtke, H., Gröger, M., Ho-Hagemann, H. T. M., Mashayekh, H., Neumann, T.,
823 and Meier, H. E. M.: Flux coupling approach on an exchange grid for the IOW Earth
824 System Model (version 1.04.00) of the Baltic Sea region, Geosci. Model Dev., 17, 1689–
825 1708, https://doi.org/10.5194/gmd-17-1689-2024, 2024.
826 Knust, R.: Polar research and supply vessel POLARSTERN operated by the Alfred-Wegener-
827 Institute. Journal of Large-Scale Research Facilities JLSRF, 3,
828 https://dx.doi.org/10.17815/jlsrf-3-163, 2017.
829 Konda, M., Imasato, N., Nishi, K., and Toda, T.: Measurement of the sea surface emissivity.
830 Journal of Oceanography, 50(1), 17–30, https://doi.org/10.1007/BF02233853, 1994.
831 Large, W. G., McWilliams, J. C., and Doney, S. C.: Oceanic vertical mixing: A review and a
832 model with a nonlocal boundary layer parameterization. Reviews of Geophysics, 32(4),
833 363–403, https://doi.org/10.1029/94RG01872, 1994.

https://doi.org/10.5194/egusphere-2026-362
Preprint. Discussion started: 10 March 2026

834 Larson, J., Jocab, R., and Ong, E.: The Model Coupling Toolkit: A New Fortran90 Toolkit for
835 Building Multiphysics Parallel Coupled Models, International Journal of High
836 Performance Computing Applications, 19(3), 277–292,
837 https://doi.org/10.1177/1094342005056115, 2005.
838 Liang, Y., Lei, R., Bi, H., and Chen, X.: Response of changes in sea ice thickness to cyclones:
839 new insights from the MOSAiC expedition. J. Climate, https://doi.org/10.1175/JCLI-D-
840 24-0765.1, 2025, in press.
841 Liepert, B. G., and Previdi, M.: Inter-model variability and biases of the global water cycle in
842 CMIP3 coupled climate models. Environ. Res. Lett., 7, 014006,
843 https://doi.org/10.1088/1748-9326/7/1/014006, 2012.
844 Liu, C., Yang, Q., Gao, Z., Shupe, M. D., Han, B., Zhang, H., Peng, S., Xi, X., and Chen, D.:
845 The role of non-local effects on surface sensible heat flux under different types of thermal
846 structures over the Arctic sea-ice surface. Geophysical Research Letters, 51,
847 e2023GL106753. https://doi.org/10.1029/2023GL106753, 2024.
848 Liu, J., Song, M., Zhu, Z., Horton, R. M., Hu, Y., and Xie, S.-P.: Arctic sea-ice loss is projected
849 to lead to more frequent strong El Niño events. Nat Commun 13, 4952,
850 https://doi.org/10.1038/s41467-022-32705-2, 2022.
851 Lei, R., Cheng, B., Hoppmann, M., and Zuo, G.: An overview of SIMBA buoys deployed in
852 the Arctic Ocean during the Legs 1a, 1, and 3 of the MOSAiC campaign in 2019-2020,
853 PANGAEA [data set], https://doi.org/10.1594/PANGAEA.938267, 2021.
854 Lei, R., Cheng, B., Hoppmann, M., Zhang, F., Zuo, G., Hutchings, J. K., Lin, L., Lan, M., Wang,
855 H., Regnery, J., Krumpen, T., Haapala, J., Rabe, B., Perovich, D. K., and Nicolaus, M.:
856 Seasonality and timing of sea ice mass balance and heat fluxes in the Arctic transpolar
857 drift during 2019–2020. Elementa Science of the Anthropocene, 10, 89.
858 https://doi.org/10.1525/elementa.2021.000089, 2022.
859 Leonard, B. and Mokhtari, S.: ULTRA-SHARP nonoscillatory convection schemes for high-
860 speed steady multidimensional flow, NASA Technical Memorandum 102568, ICOMP-

https://doi.org/10.5194/egusphere-2026-362
Preprint. Discussion started: 10 March 2026

90-12, 54 pp., https://ntrs.nasa.gov/citations/19900012254 (last access: 30 Nov 2025), 1990.

Lucarini, V., and Ragone, F.: Energetics of climate models: Net energy balance and meridional enthalpy transport. Rev. Geophys., 49, RG1001, https://doi.org/10.1029/2009RG000323, 2011.

Maturilli, M., Sommer, M., Holdridge, D. J., Dahlke, S., Graeser, J., Sommerfeld, A., Jaiser, R., Deckelmann, H., and Schulz, A.: MOSAiC radiosonde data (level 3), PANGAEA [data set], https://doi.org/10.1594/PANGAEA.943870, 2022.

Maykut, G. A. and McPhee. M. G.: Solar heating of the Arctic mixed layer, J. Geophys. Res.-Oceans, 100, 24691–24703, http://doi.org/10.1029/95JC02554, 1995.

Meier, W. N., Petty, A., Hendricks, S., Bliss, A., Kaleschke, L., Divine, D., Farrell, S., Gerland, S., Perovich, D., Ricker, R., Tian-Kunze, X., and Webster M.: Sea Ice. Arctic Report Card 2024, Moon, T. A., Druckenmiller, M. L., and Thoman, R. L., Eds., https://doi.org/10.25923/aksk-7p66, 2024.

Morrison, H., Thompson, G., and Tatarskii, V.: Impact of Cloud Microphysics on the Development of Trailing Stratiform Precipitation in a Simulated Squall Line: Comparison of One– and Two–Moment Schemes. Mon. Wea. Rev., 137, 991-1007. https://doi.org/10.1175/2008MWR2556.1, 2009.

Nakanishi, M., and Niino., H.: Development of an improved turbulence closure model for the atmospheric boundary layer. J. Meteor. Soc. Japan, 87, 895–912, https://doi.org/10.2151/jmsj.87.895, 2009.

Nicolaus, M., Perovich, D., Spreen, G., Granskog, M., Albedyll, L., Angelopoulos, M., Anhaus, P., Arndt, S., Belter, H., Bessonov, V., Birnbaum, G., Brauchle, J., Calmer, R., Cardellach, E., Cheng, B., Clemens-Sewall, D., Dadic, R., Damm, E., de Boer, G., Demir, O., Dethloff, K., Divine, D., Fong, A., Fons, S., Frey, M., Fuchs, N., Gabarró, C., Gerland, S., Goessling, H., Gradinger, R., Haapala, J., Haas, C., Hamilton, J., Hannula, H.-R., Hendricks, S., Herber, A., Heuzé, C., Hoppmann, M., Høyland, K., Huntemann, M., Hutchings, J.,

https://doi.org/10.5194/egusphere-2026-362
Preprint. Discussion started: 10 March 2026

Hwang, B., Itkin, P., Jacobi, H.-W., Jaggi, M., Jutila, A., Kaleschke, L., Katlein, C., Kolabutin, N., Krampe, D., Kristensen, S., Krumpen, T., Kurtz, N., Lampert, A., Lange, B., Lei, R., Light, B., Linhardt, F., Liston, G., Loose, B., Macfarlane, A., Mahmud, M., Matero, I., Maus, S., Morgenstern, A., Naderpour, R., Nandan, V., Niubom, A., Oggier, M., Oppelt, N., Pätzold, F., Perron, C., Petrovsky, T., Pirazzini, R., Polashenski, C., Rabe, B., Raphael, I., Regnery, J., Rex, M., Ricker, R., Riemann-Campe, K., Rinke, A., Rohde, J., Salganik, E., Scharien, R., Schiller, M., Schneebeli, M., Semmling, M., Shimanchuk, E., Shupe, M., Smith, M., Smolyanitsky, V., Sokolov, V., Stanton, T., Stroeve, J., Thielke, L., Timofeeva, A., Tonboe, R., Tavri, A., Tsamados, M., Wagner, D., Watkins, D., Webster, M., and Wendisch, M.: Overview of the MOSAiC expedition – Snow and sea ice, Elementa, 10, 000046, https://doi.org/10.1525/elementa.2021.000046, 2022.

Notz, D., Jahn, A., Holland, M., Hunke, E., Massonnet, F., Stroeve, J., Tremblay, B., and Vancoppenolle, M.: The CMIP6 Sea-Ice Model Intercomparison Project (SIMIP): understanding sea ice through climate-model simulations, Geosci. Model Dev., 9, 3427-3446, https://doi.org/10.5194/gmd-9-3427-2016, 2016.

Polyakov, I. V., Pnyushkov, A. V., Alkire, M. B., Ashik, I. M., Baumann, T. M., Carmack, E. C., Goszczko, I., Guthrie, J., Ivanov, V. V., Kanzow, T., Krishfield, R., Kwok, R., Sundfjord, A., Morison, J., Rember, R., and Yulin, A.: Greater role for Atlantic inflows on sea-ice loss in the Eurasian Basin of the Arctic Ocean. Science 356, 285–291, https://doi.org/10.1126/science.aai8204, 2017.

Polyakov, I. V, Ingvaldsen, R. B., Pnyushkov, A. V., Bhatt, U. S., Francis, J. A., Janout, M., Kwok, R., and Skagseth, Ø: Fluctuating Atlantic inflows modulate Arctic atlantification. Science, 381, 972-979, https://doi.org/10.1126/science.adh5158, 2023.

Rabe, B., Heuzé, C., Regnery, J., Aksenov, Y., Allerholt, J., Athanase, M., Bai, Y., Basque, C., Bauch, D., Baumann, T. M., Chen, D., Cole, S. T., Craw, L., Davies, A., Damm, E., Dethloff, K., Divine, D. V., Doglioni, F., Ebert, F., Fang, Y.-C., Fer, I., Fong, A. A., Gradinger, R., Granskog, M. A., Graupner, R., Haas, C., He, H., He, Y., Hoppmann, M.,

https://doi.org/10.5194/egusphere-2026-362
Preprint. Discussion started: 10 March 2026

Janout, M., Kadko, D., Kanzow, T., Karam, S., Kawaguchi, Y., Koenig, Z., Kong, B., Krishfield, R. A., Krumpen, T., Kuhlmey, D., Kuznetsov, I., Lan, M., Laukert, G., Lei, R., Li, T., Torres-Valdés, S., Lin, L., Lin, L., Liu, H., Liu, N., Loose, B., Ma, X., McKay, R., Mallet, M., Mallett, R. D. C., Maslowski, W., Mertens, C., Mohrholz, V., Muilwijk, M., Nicolaus, M., O'Brien, J. K., Perovich, D., Ren, J., Rex, M., Ribeiro, N., Annette, A., Schaffer, J., Schuffenhauer, I., Schulz, K., Shupe, M. D., Shaw, W., Sokolov, V., Sommerfeld, A., Spreen, G., Stanton, T., Stephens, M., Su, J., Sukhikh, N., Sundfjord, A., Thomisch, K., Tippenhauer, S., Toole, J. M., Vredenborg, M., Walter, M., Wang, H., Wang, L., Wang, Y., Wendisch, M., Zhao, J., Zhou, M., and Zhu, J.: Overview of the MOSAiC expedition: Physical oceanography, Elementa, 10, 00062, https://doi.org/10.1525/elementa.2021.00062, 2022.

Rahmstorf, S.: Climate drift in an ocean model coupled to a simple, perfectly matched atmosphere. Climate Dyn., 11, 447–458, https://doi.org/10.1007/BF00207194, 1995.

Rantanen, M., Karpechko, A. Y., Lipponen, A., Nordling, K., Hyvärinen, O., Ruosteenoja, K., Vihma, T., and Laaksonen, A.: The Arctic has warmed nearly four times faster than the globe since 1979. Commun Earth Environ 3, 168, https://doi.org/10.1038/s43247-022-00498-3, 2022.

Ricker, R., Hendricks, S., Kaleschke, L., Tian-Kunze, X., King, J., and Haas, C.: A weekly Arctic sea-ice thickness data record from merged CryoSat-2 and SMOS satellite data, The Cryosphere, 11, 1607–1623, https://doi.org/10.5194/tc-11-1607-2017, 2017.

Rinke, A, Cassano, J. J., Cassano, E. N., Jaiser, R., and Handorf, D.: Meteorological conditions during the MOSAiC expedition: Normal or anomalous?. Elem Sci Anth, 9:1, https://doi.org/10.1525/elementa.2021.00023, 2021.

Roach, L. A., and Meier, W. N.: Sea ice in 2024. Nat. Rev. Earth Environ., 6, 252–254, https://doi.org/10.1038/s43017-025-00662-1, 2025.

https://doi.org/10.5194/egusphere-2026-362
Preprint. Discussion started: 10 March 2026

940 Screen, J., and Simmonds, I.: The central role of diminishing sea ice in recent Arctic
941 temperature amplification. Nature, 464, 1334–1337, https://doi.org/10.1038/nature09051,
942 2010.
943 Sedlar, J., Tjernström, M., Rinke, A., Orr, A., Cassano, J., Fettweis, X., Heinemann, G.,
944 Seefeldt, M., Solomon, A., Matthes, H., Phillips, T., and Webster, S.: Confronting Arctic
945 troposphere, clouds, and surface energy budget representations in regional climate models
946 with observations. Journal of Geophysical Research: Atmospheres, 125.
947 https://doi.org/10.1029/2019JD031783, 2020.
948 Shapiro, R.: Smoothing, filtering, and boundary effects, Rev. Geophys., 8(2), 359–387,
949 https://doi.org/10.1029/RG008i002p00359, 1970.
950 Shchepetkin, A. F., and McWilliams, J. C.: The Regional Ocean Modeling System: A split-
951 explicit, free-surface, topography following coordinates ocean model, Ocean Modelling,
952 9, 347-404, https://doi.org/10.1016/j.ocemod.2004.08.002, 2005.
953 Shupe, M. D. and Intrieri, J. M.: Cloud Radiative Forcing of the Arctic Surface: The Influence
954 of Cloud Properties, Surface Albedo, and Solar Zenith Angle, J. Climate, 17, 616–628,
955 https://doi.org/10.1175/1520-0442(2004)017<0616:CRFOTA>2.0.CO;2, 2004.
956 Shupe, M. D.: ShupeTurner cloud microphysics product, ARM Mobile Facility (MOS)
957 MOSAiC (Drifting Obs – Study of Arctic Climate), ARM Data Center [data set],
958 https://doi.org/10.5439/1871015, 2022.
959 Shupe, M. D., Rex, M., Blomquist, B., Persson, P. O. G., Schmale, J., Uttal, T., Althausen, D.,
960 Angot, H., Archer, S., Bariteau, L., Beck, I., Bilberry, J., Bucci, S., Buck, C., Boyer, M.,
961 Brasseur, Z., Brooks, I. M., Calmer, R., Cassano, J., Castro, V., Chu, D., Costa, D., Cox,
962 C. J., Creamean, J., Crewell, S., Dahlke, S., Damm, E., de Boer, G., Deckelmann, H.,
963 Dethloff, K., Dütsch, M., Ebell, K., Ehrlich, A., Ellis, J., Engelmann, R., Fong, A. A., Frey,
964 M. M., Gallagher, M. R., Ganzeveld, L., Gradinger, R., Graeser, J., Greenamyer, V.,
965 Griesche, H., Griffiths, S., Hamilton, J., Heinemann, G., Helmig, D., Herber, A., Heuzé,
966 C., Hofer, J., Houchens, T., Howard, D., Inoue, J., Jacobi, H.-W., Jaiser, R., Jokinen, T.,

https://doi.org/10.5194/egusphere-2026-362
Preprint. Discussion started: 10 March 2026

967 Jourdan, O., Jozef, G., King, W., Kirchgaessner, A., Klingebiel, M., Krassovski, M.,
968 Krumpen, T., Lampert, A., Landing, W., Laurila, T., Lawrence, D., Lonardi, M., Loose,
969 B., Lüpkes, C., Maahn, M., Macke, A., Maslowski, W., Marsay, C., Maturilli, M., Mech,
970 M., Morris, S., Moser, M., Nicolaus, M., Ortega, P., Osborn, J., Pätzold, F., Perovich, D.
971 K., Petäjä, T., Pilz, C., Pirazzini, R., Posman, K., Powers, H., Pratt, K. A., Preußer, A.,
972 Quéléver, L., Radenz, M., Rabe, B., Rinke, A., Sachs, T., Schulz, A., Siebert, H., Silva, T.,
973 Solomon, A., Sommerfeld, A., Spreen, G., Stephens, M., Stohl, A., Svensson, G., Uin, J.,
974 Viegas, J., Voigt, C., von der Gathen, P., Wehner, B., Welker, J. M., Wendisch, M., Werner,
975 M., Xie, Z. Q., and Yue, F.: Overview of the MOSAiC expedition: Atmosphere, Elementa,
976 10, 00060, https://doi.org/10.1525/elementa.2021.00060, 2022.
977 Simmonds, I., and Rudeva, I.: The great Arctic cyclone of August 2012, Geophys. Res. Lett.,
978 39, L23709, https://doi.org/10.1029/2012GL054259, 2012.
979 Tan, I., Sotiropoulou, G., Taylor, P. C., Zamora, L. and Wendisch, M.: A Review of the Factors
980 Influencing Arctic Mixed-Phase Clouds: Progress and Outlook. In Clouds and Their
981 Climatic Impacts, Sullivan, S. C. and Hoose, C., Eds.,
982 https://doi.org/10.1002/9781119700357.ch5, 2023.
983 Timmermans, M.-L., and Toole, J. M.: the Arctic Ocean's Beaufort Gyre. Ann. Rev. Mar. Sci.
984 15, 223–248, https://doi.org/10.1146/annurev-marine-032122-012034, 2023.
985 Turner, A. K., and Hunke, E. C.: Impacts of a mushy-layer thermodynamic approach in global
986 sea-ice simulations using the CICE sea-ice model, J. Geophys. Res. Oceans, 120, 1253-
987 1275, https://doi.org/10.1002/2014JC010358, 2015.
988 Uttal, T., Curry, J. A., McPhee, M. G., Perovich, D. K., Moritz, R. E., Maslanik, J. A., Guest,
989 P. S., Stern, H. L., Moore, J. A., Turenne, R., Heiberg, A., Serreze, M. C., Wylie, D. P.,
990 Persson, O. G., Paulson, C. A., Halle, C., Morison, J. H., Wheeler, P. A., Makshtas,
991 A.,Welch, H., Shupe, M. D., Intrieri, J. M., Stamnes, K., Lindsay, R. W., Pinkel, R., Pegau,
992 W. S., Stanton, T. P., Grenfeld, T. C.: The surface heat budget of the Arctic. Bulletin of the

https://doi.org/10.5194/egusphere-2026-362
Preprint. Discussion started: 10 March 2026

American Meteorological Society 83: 255–275, https://dx.doi.org/10.1175/1520-0477(2002)083<0255:SHBOTA>2.3.CO;2, 2002.

Wang Q., Shu. Q., and Wang F.: Recent emergence of Arctic atlantification dominated by climate warming. Sci. Adv. 10, eadq5235 https://doi.org/10.1126/sciadv.adq5235, 2024.

Wang, Q., Shu, Q., Wang, S., Li, X., Danilov, S., Qiao, F., Song, Z., Wang, F., and Jung, T.: Dominant inflation of the Arctic Ocean's Beaufort Gyre in a warming climate. Commun Earth Environ 6, 40, https://doi.org/10.1038/s43247-025-02028-3, 2025.

Warren, S. G.: Optical properties of ice and snow. Phil. Trans. R. Soc. A., 37720180161, http://doi.org/10.1098/rsta.2018.0161, 2019.

Yang, C.-Y.: The evalutaion data utilized in the manuscript: "Conservation of Heat in the Coupled Arctic Prediction System (CAPS v1.1): Comprehensive model evaluation based on the MOSAiC observations" [Data set]. Zenodo. https://doi.org/10.5281/zenodo.18764432, 2026a.

Yang, C.-Y.: The model code of Coupled Arctic Prediction System version 1.1 (CAPS v1.1) for the permanent archive in the manuscript: "Conservation of Heat in the Coupled Arctic Prediction System (v1.1): Comprehensive model evaluation based on the MOSAiC observations", Zenodo [code], https://doi.org/10.5281/zenodo.18308943, 2026b.

Yang, C.-Y.: The simulated outputs analyzed in the manuscript: "Conservation of Heat in the Coupled Arctic Prediction System (v1.1): Comprehensive model evaluation based on the MOSAiC observations", Zenodo [data set], https://doi.org/10.5281/zenodo.18308549, 2026c.

Yang, C.-Y., Liu, J., and Xu, S.: Seasonal Arctic sea ice prediction using a newly developed fully coupled regional model with the assimilation of satellite sea ice observations, J. Adv. Model. Earth Sy., 12, e2019MS001938, https://doi.org/10.1029/2019MS001938, 2020.

Yang, C.-Y., Liu, J., and Chen, D.: An improved regional coupled modeling system for Arctic sea ice simulation and prediction: a case study for 2018, Geosci. Model Dev., 15, 1155–1176, https://doi.org/10.5194/gmd-15-1155-2022, 2022.

https://doi.org/10.5194/egusphere-2026-362
Preprint. Discussion started: 10 March 2026

Yang, C.-Y., Liu, J., and Chen, D.: Understanding the influence of ocean waves on Arctic sea ice simulation: a modeling study with an atmosphere–ocean–wave–sea ice coupled model, The Cryosphere, 18, 1215–1239, https://doi.org/10.5194/tc-18-1215-2024, 2024.

Yao, C., Yan, Y., Zhou, Y., Xiong, Z., Xu, Y., and Uotila, P.: Comparative analysis of multiple ocean reanalysis datasets in the Arctic. Clim Dyn, 63, 347, https://doi.org/10.1007/s00382-025-07842-1, 2025.

Zhang, J. and Rothrock, D.: Modeling global sea ice with a thickness and enthalpy distribution model in generalized curvilinear coordinates. Mon. Wea. Rev., 131, 845–861, https://doi.org/10.1175/1520-0493(2003)131<0845:MGSIWA>2.0.CO;2, 2003.

Zhang, J., Weijer, W., Steele, M., Cheng, W., Verma, T., and Venezaini, M.: Labrador Sea freshening linked to Beaufort Gyre freshwater release. Nat. Commun., 12, 1229, https://doi.org/10.1038/s41467-021-21470-3, 2021.

https://doi.org/10.5194/egusphere-2026-362
Preprint. Discussion started: 10 March 2026

6. Tables

Table 1 List of exchanged variables in CAPS with the revised coupling approach.

Variable	Source	Destination	Meaning
F_{swdn}	WRF	ROMS, CICE	Downward shortwave radiation at the surface
F_{lwdn}	WRF	ROMS, CICE	Downward longwave radiation at the surface
$F_{sh,ao}$	WRF	ROMS	Sensible heat flux at the atmosphere–ocean interface
$F_{lh,ao}$	WRF	ROMS	Latent heat flux at the atmosphere–ocean interface
$\vec{\tau}_{ao}$	WRF	ROMS	Wind stress at the atmosphere–ocean interface
$MSLP$	WRF	ROMS	Mean sea level pressure
z_a	WRF	CICE	Height of the lowest atmospheric level
θ_a	WRF	CICE	Potential temperature at the lowest atmospheric level
Q_a	WRF	CICE	Specific humidity at the lowest atmospheric level
$\vec{U}_a$	WRF	CICE	Wind fields at the lowest atmospheric level
P_{total}	WRF	ROMS, CICE	Total precipitation rate
E_{ao}	WRF	ROMS	Evaporation rate at the atmosphere–ocean interface
SST	ROMS	WRF, CICE	Sea surface temperature
SSS	ROMS	CICE	Sea surface salinity
W_{fr}	ROMS	CICE	Freezing/melting potential
$\vec{U}_o$	ROMS	CICE	Surface ocean currents
∇H_o	ROMS	CICE	Sea surface slope
A_{ice}	CICE	WRF	Sea ice concentration
T_{ice}	CICE	WRF	Ice surface temperature
α_{ice}	CICE	WRF	Surface albedo of snow and ice
$F_{sh,ai}$	CICE	WRF	Sensible heat flux at the atmosphere–ice interface
$F_{lh,ai}$	CICE	WRF	Latent heat flux at the atmosphere–ice interface
$F_{swthru,io}$	CICE	ROMS	Penetrated shortwave radiation through sea ice
$F_{heat,io}$	CICE	ROMS	Net heat flux at the ice–ocean interface
$F_{water,io}$	CICE	ROMS	Freshwater flux at the ice–ocean interface
$F_{salt,io}$	CICE	ROMS	Salt flux at the ice–ocean interface
$\vec{\tau}_{io}$	CICE	ROMS	Ice–ocean stress

https://doi.org/10.5194/egusphere-2026-362
Preprint. Discussion started: 10 March 2026

1037 Table 2 The summary of physic options and details of the revised CAPS.

Horizontal grid points	320 x grid points * 440 y grid points
Horizontal grid spacing	~24 km
Vertical layers	WRF: 50 with 10 hPa as the model top ROMS: 40 CICE: 7 ice layers, 1 snow layer
Time step	WRF: 60 s WRF radiation calling interval: 15 min ROMS/CICE: 180 s Coupling frequency: 180 s
WRF physics	
Cumulus	Grell-Freitas (Freitas et al. 2018)
Microphysics	Morrison 2-moment (Morrison et al. 2009)
Longwave radiation	RRTMG (Iacono et al., 2008)
Shortwave radiation	RRTMG (Iacono et al., 2008)
Boundary layer	MYNN Level 2.5 (Nakanishi and Niino, 2006)
Land surface	Unified Noah LSM (Chen and Dudhia 2001)
ROMS physics	
Tracer advection	Upwind third-order horizontal advection with the upwind flux limiter (Leonard and Mokhtari, 1990; Shchepetkin, and McWilliams, 2005) Centered fourth-order vertical advection (Shchepetkin, and McWilliams, 2005)
Tracer vertical mixing	KPP (Large et al., 1994)
CICE physics	
Ice dynamics	EVP (Hunke and Dukowicz, 1997)
Ice thermodynamics	Bitz and Lipscomb (1999)
Shortwave albedo	Delta-Eddington (Briegleb and Light, 2007)
Melt pond	Level-ice (Hunke et al., 2013)

1038
1039

https://doi.org/10.5194/egusphere-2026-362
Preprint. Discussion started: 10 March 2026

7. Figures

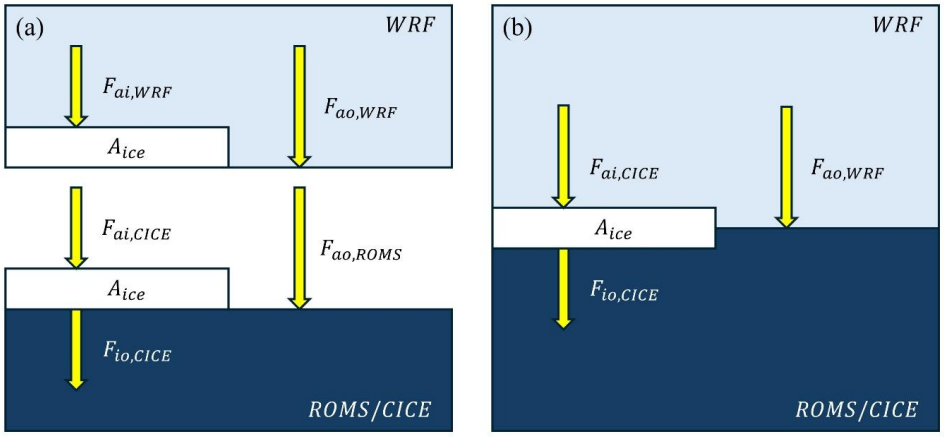

Figure 1 Pathways of surface heat fluxes exchange between WRF and ROMS/CICE in CAPS for (a) the original coupling approach, and (b) the revised coupling approach.

https://doi.org/10.5194/egusphere-2026-362
Preprint. Discussion started: 10 March 2026

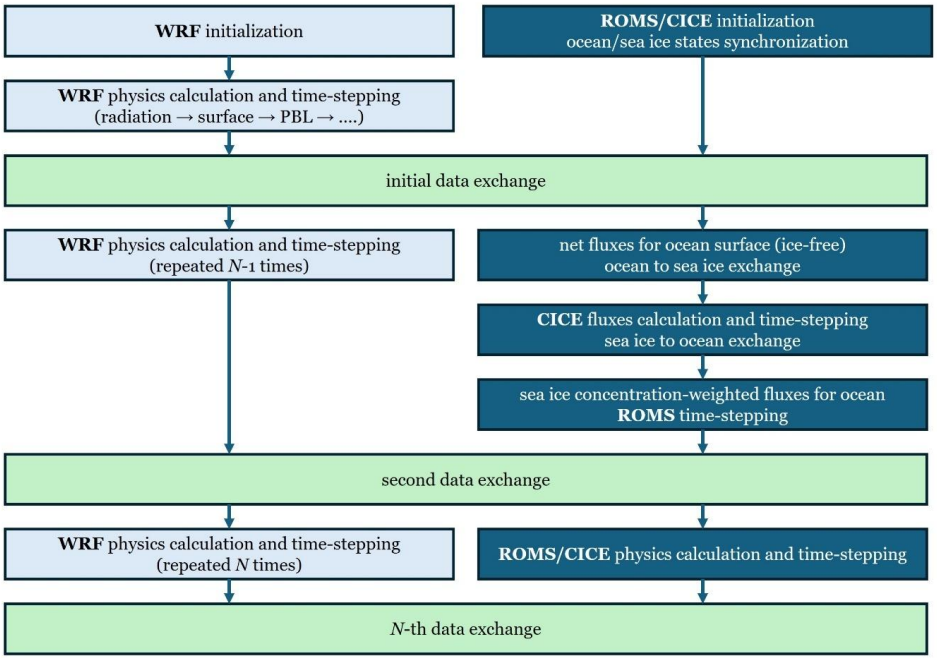

Figure 2 Schematic model sequence diagram for coupling between WRF and ROMS/CICE. The steps taken in WRF and ROMS/CICE are visualized as the light blue and dark blue blocks. The variable exchange is represented as the light green block.

https://doi.org/10.5194/egusphere-2026-362
Preprint. Discussion started: 10 March 2026

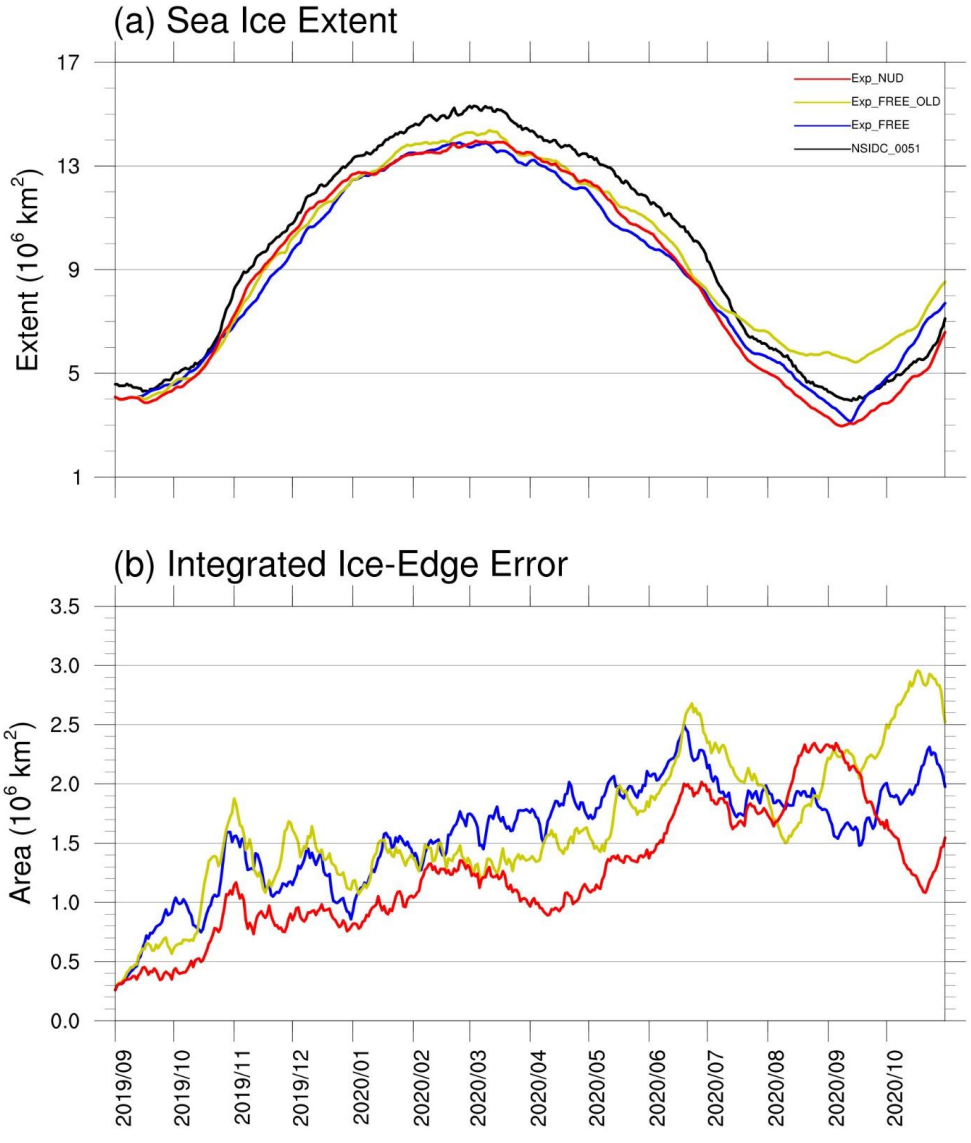

Figure 3 Time-series of (a) Arctic sea ice extent for the observations (NSIDC-0051, black line), Exp_FREE_OLD (yellow line), Exp_FREE (blue line), and Exp_NUD (red line), and (b) integrated ice-edge error for Exp_FREE_OLD, Exp_FREE, and Exp_NUD.

https://doi.org/10.5194/egusphere-2026-362
Preprint. Discussion started: 10 March 2026

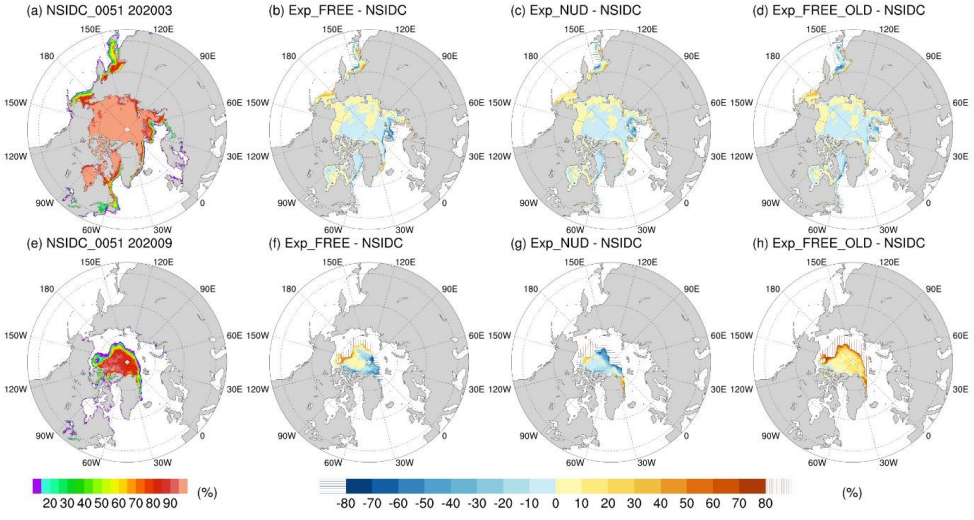

Figure 4 The monthly averaged sea ice concentration for the observations in (a) March 2020, and (e) September 2020, and the difference between the experiments and the observations for Exp_FREE, Exp_NUD, and Exp_FREE_OLD in (b-d) March 2020, and (f-h) September 2020. Note: vertical/horizontal-lining represents the overestimated/underestimated local sea ice extent (OLSIE/ULSIE) with respect to the observed local sea ice extent, same as the definition of IIEE (Goessling et al., 2016).

https://doi.org/10.5194/egusphere-2026-362
Preprint. Discussion started: 10 March 2026

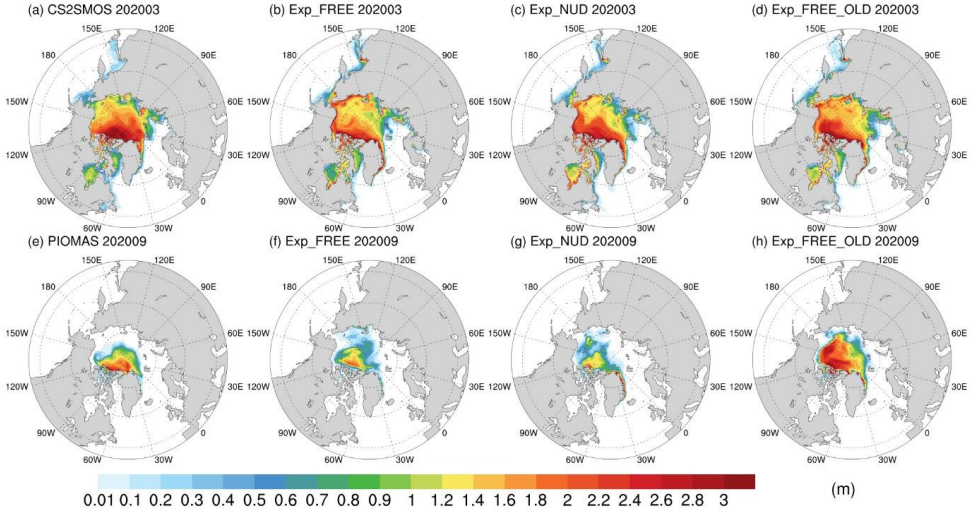

Figure 5 The monthly averaged sea ice thickness for the reference data, Exp_FREE, Exp_NUD, and Exp_FREE_OLD in (a-d) March 2020, and (e-h) September 2020.

https://doi.org/10.5194/egusphere-2026-362
Preprint. Discussion started: 10 March 2026

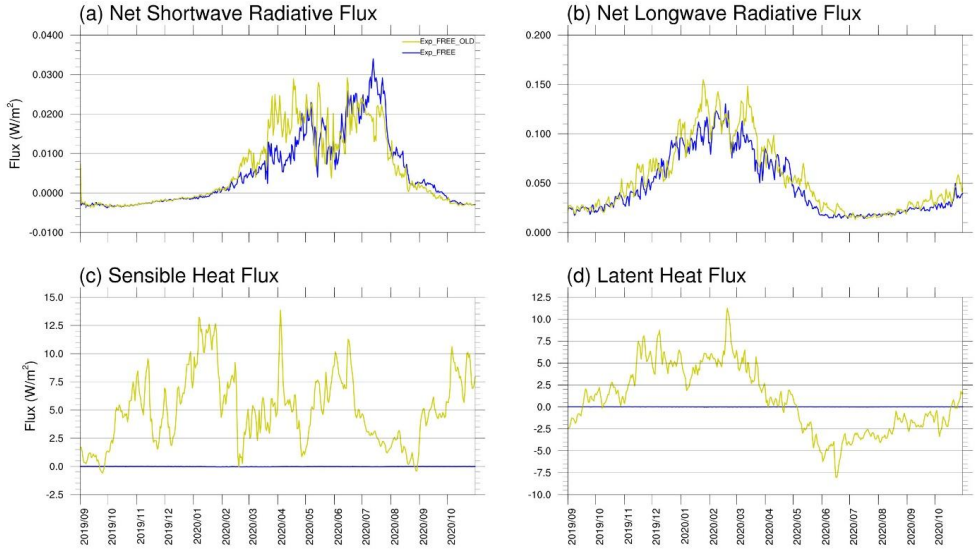

Figure 6 Differences between WRF and ROMS/CICE sides of (a) net shortwave radiative flux, (b) net longwave radiative flux, (c) sensible heat flux, and (d) latent heat flux averaged over all open-ocean and ice-covered cells for Exp_FREE (blue line) and Exp_FREE_OLD (yellow line). Note: all fluxes are defined as positive downwards.

https://doi.org/10.5194/egusphere-2026-362
Preprint. Discussion started: 10 March 2026

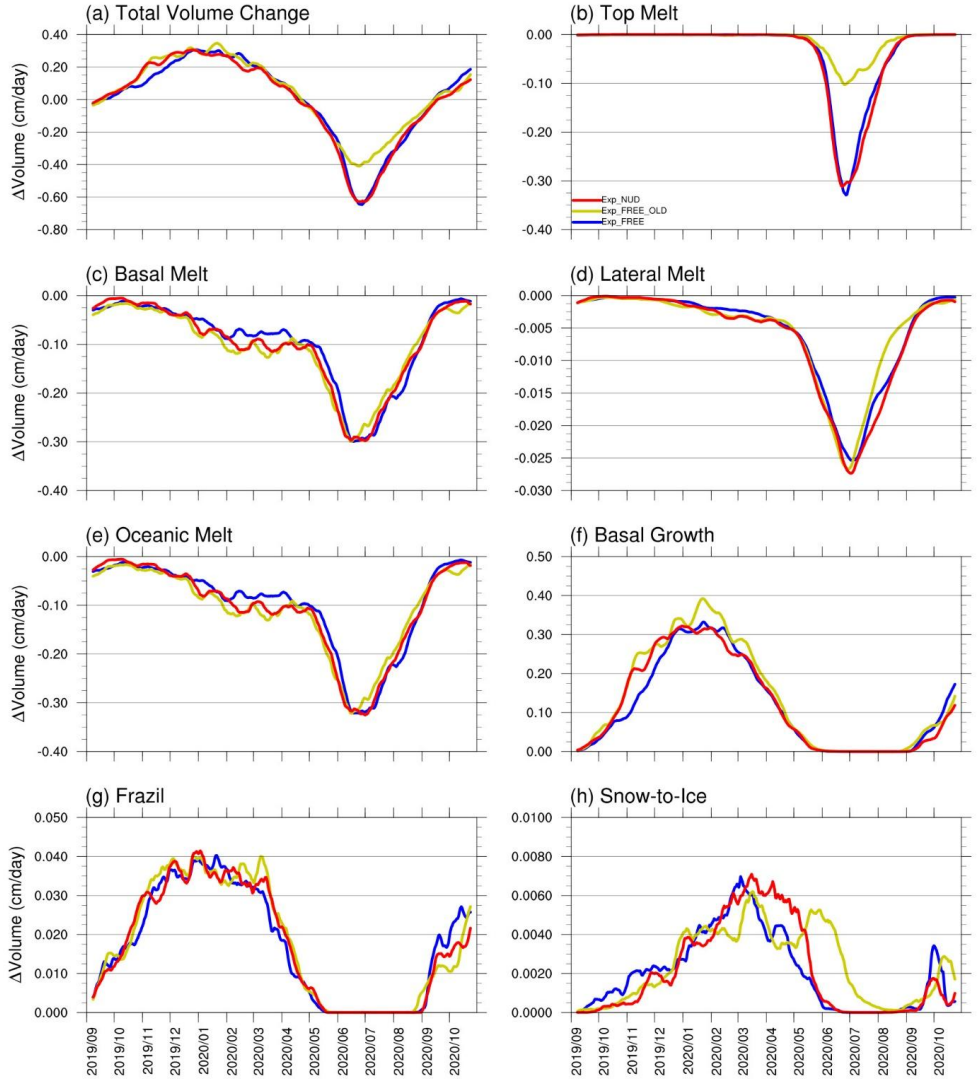

Figure 7 Time-series (15-day running-averaged) of sea ice volume budget for Exp_FREE (blue line), Exp_FREE_OLD (yellow line), and Exp_NUD (red line). Sea ice volume budgets include: (a) total volume change, (b) sea ice melt at the air-ice interface (top melt), (c) sea ice melt at the bottom of the ice (basal melt), (d) sea ice melt at the sides of the ice (lateral melt), (e) sea ice melt from oceanic energy (basal plus lateral melt), (f) sea ice growth at the bottom of the ice (basal growth), (g) sea ice growth by supercooled open water (frazil), and (h) sea ice growth due to transformation of snow to sea ice (snowice). Note: (a)-(h) are averaged over the model domain (Fig. S1).

https://doi.org/10.5194/egusphere-2026-362
Preprint. Discussion started: 10 March 2026

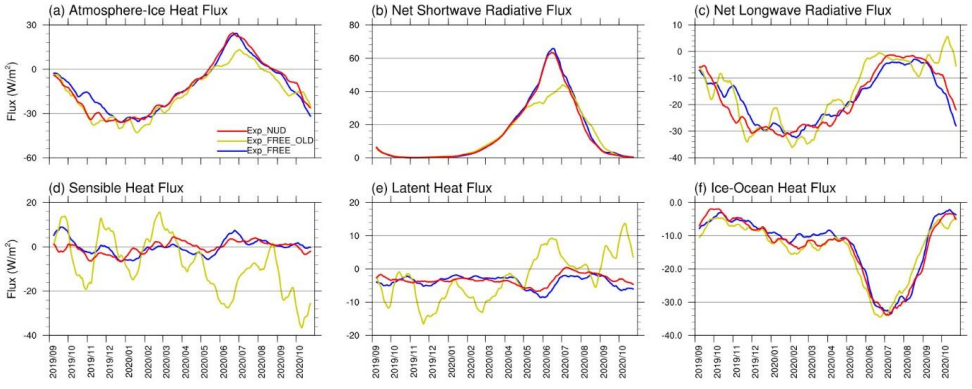

Figure 8 Time-series (15-day running-averaged) of (a) atmosphere–ice heat flux, (b) net shortwave radiative flux, (c) net longwave radiative flux, (d) sensible heat flux, (e) latent heat flux, and (f) ice–ocean heat flux for Exp_FREE (blue line), Exp_FREE_OLD (yellow line), and Exp_NUD (red line). Note: (a)-(f) are averaged with SIC-weighting over all grid cells with at least 1% SIC (Fig. S1) to represent the mean value of the grid cell, are defined as positive downwards.

https://doi.org/10.5194/egusphere-2026-362
Preprint. Discussion started: 10 March 2026

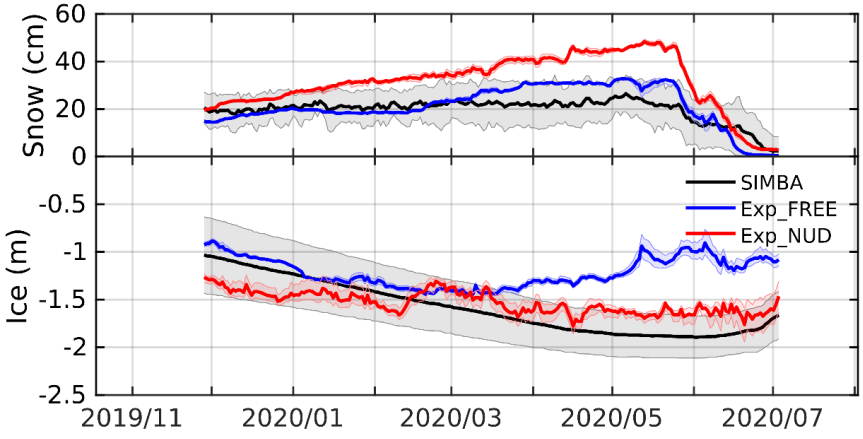

Figure 9 Time-series of daily-mean snow depth (upper box) and sea ice thickness (lower box) for SIMBA buoys (black line), Exp_FREE (blue line), and Exp_NUD (red line) along the track of MOSAiC drift. Note: the shadings represent the uncertainty range of the simulated and observed variables. For SIMBA buoys, the uncertainty range is plus/minus one standard deviation. For the simulations, the uncertainty range is the range of the nearest grid cell to the observed latitude/longitude and four nearby grid cells.

https://doi.org/10.5194/egusphere-2026-362
Preprint. Discussion started: 10 March 2026

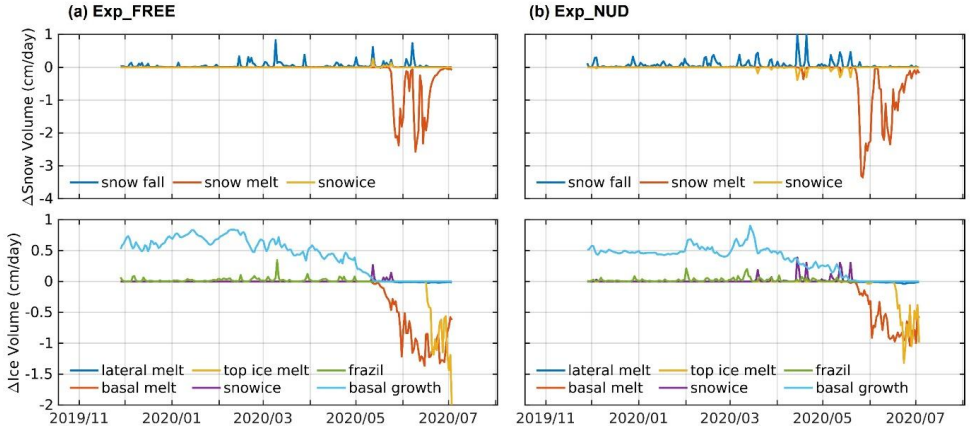

Figure 10 Time-series of snow (upper boxes) and sea ice (bottom boxes) volume budget for (a) Exp_FREE, and (b) Exp_NUD along the track of the SIMBA buoys.

https://doi.org/10.5194/egusphere-2026-362
Preprint. Discussion started: 10 March 2026

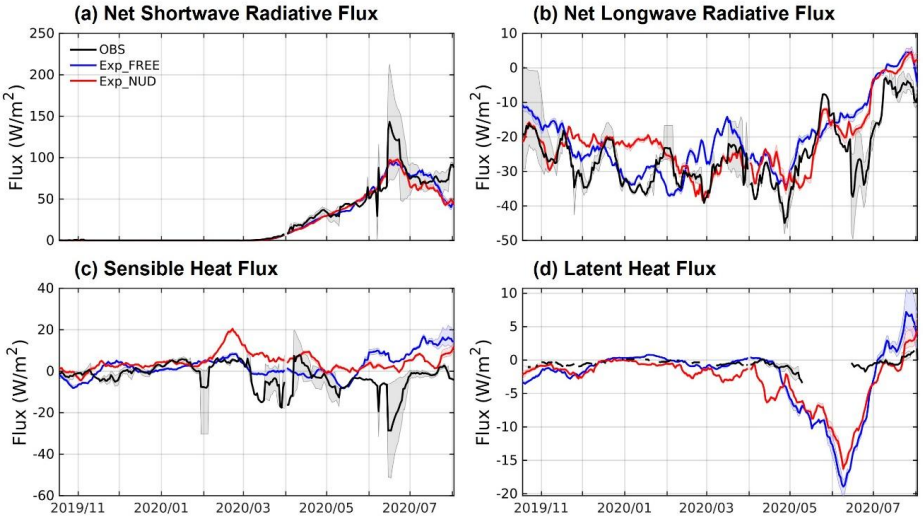

Figure 11 Time-series (15-day running-averaged) of (a) net shortwave radiative flux, (b) net longwave radiative flux, (c) sensible heat flux, and (d) latent heat flux for the observations (black line), Exp_FREE (blue line), and Exp_NUD (red line) along the track of MOSAiC drift. Note: all fluxes are defined as positive downwards. The shadings represent the uncertainty range of the simulated and observed variables. For the observations, the uncertainty range is the range of available sites with non-missing values. For the simulations, the uncertainty range is the range of the nearest grid cell to the observed latitude/longitude and four nearby grid cells.

https://doi.org/10.5194/egusphere-2026-362
Preprint. Discussion started: 10 March 2026

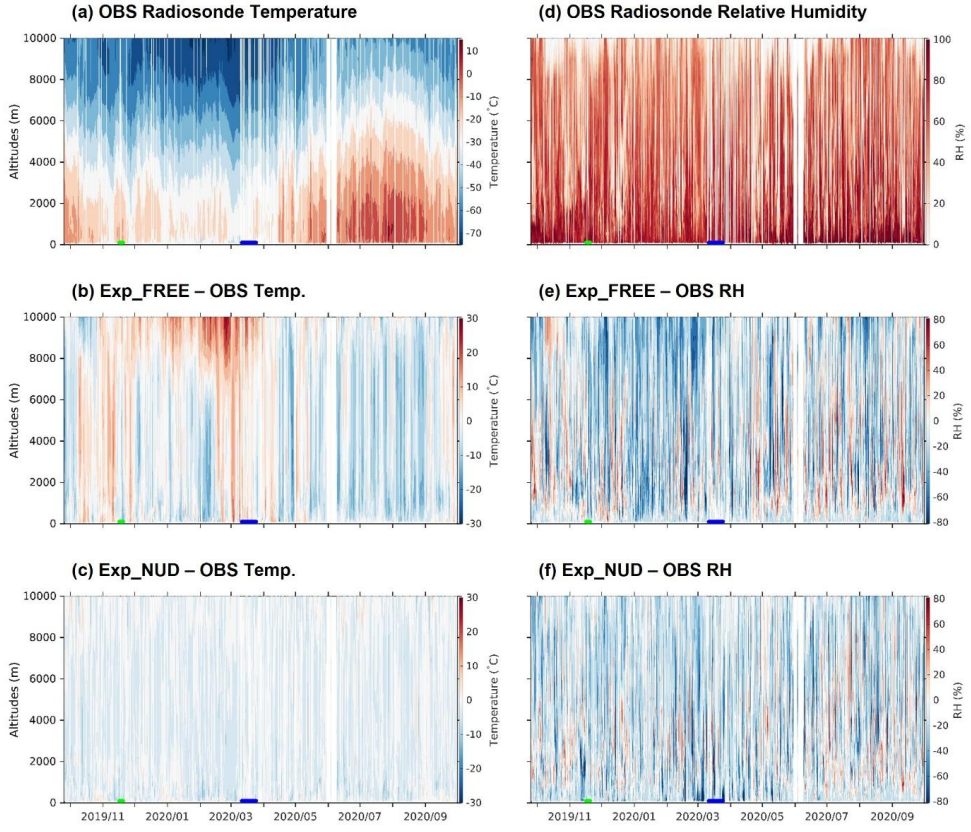

Figure 12 The evolutions of (a) atmospheric temperature profile, and (d) relative humidity profile observed by the radiosondes, and the temperature and relative humidity profile difference between the experiments and the observations for (b, e) Exp_FREE, and (c, f) Exp_NUD along the track of MOSAiC drift. Note: green and blue lines on time-axis represent the STORM-1 and STORM-2 periods.

https://doi.org/10.5194/egusphere-2026-362
Preprint. Discussion started: 10 March 2026

1122

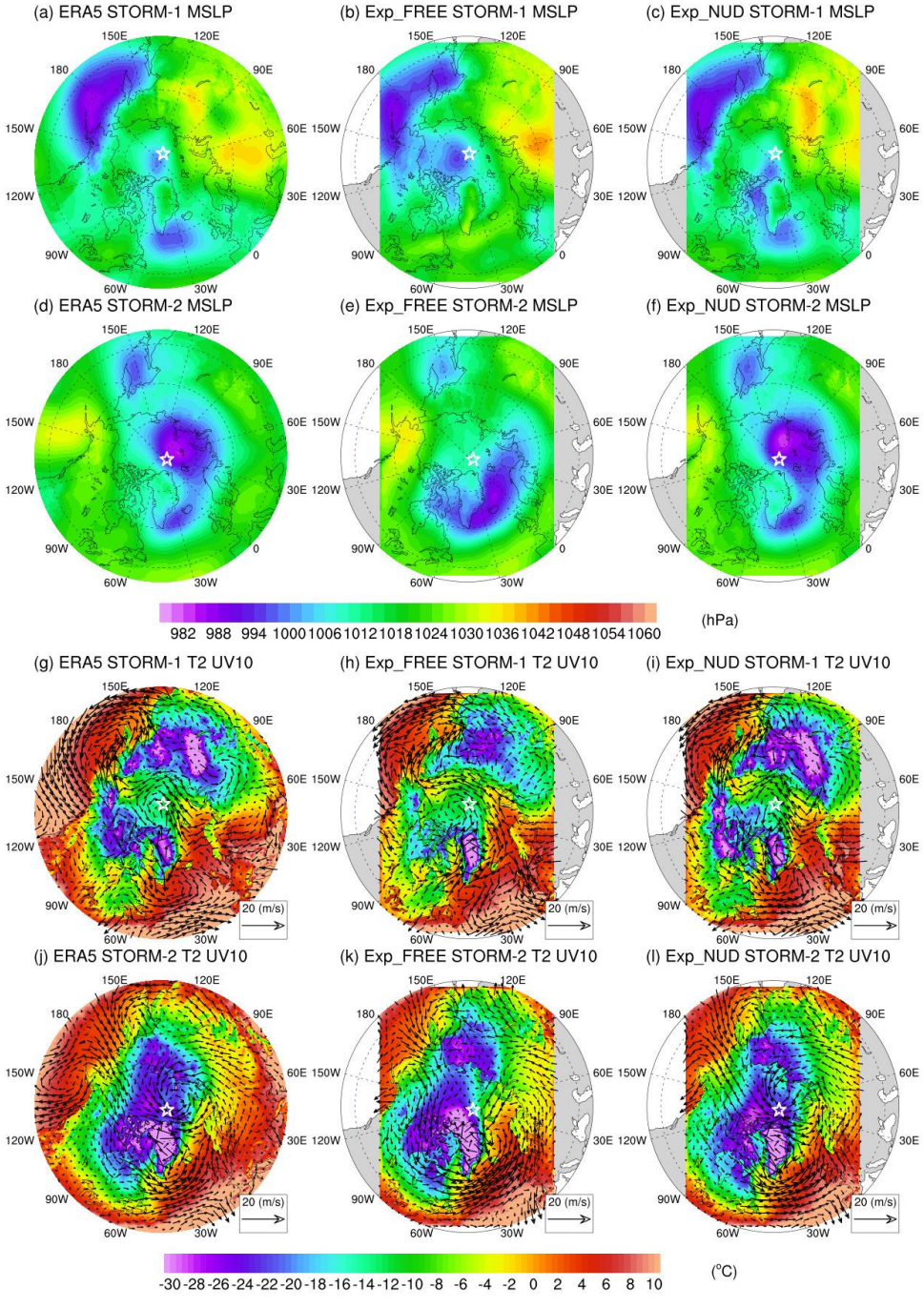

1123

https://doi.org/10.5194/egusphere-2026-362
Preprint. Discussion started: 10 March 2026

Figure 13 The averaged mean sea level pressure of (a, d) ERA5, (b, e) Exp_FREE, and (c, f) Exp_NUD, and the averaged near surface temperature and wind fields of (g, j) ERA5, (h, k) Exp_FREE, and (i, l) Exp_NUD during the period of STORM-1 and STORM-2. Note: white star represents the averaged location of radiosondes during the corresponding period.

https://doi.org/10.5194/egusphere-2026-362
Preprint. Discussion started: 10 March 2026

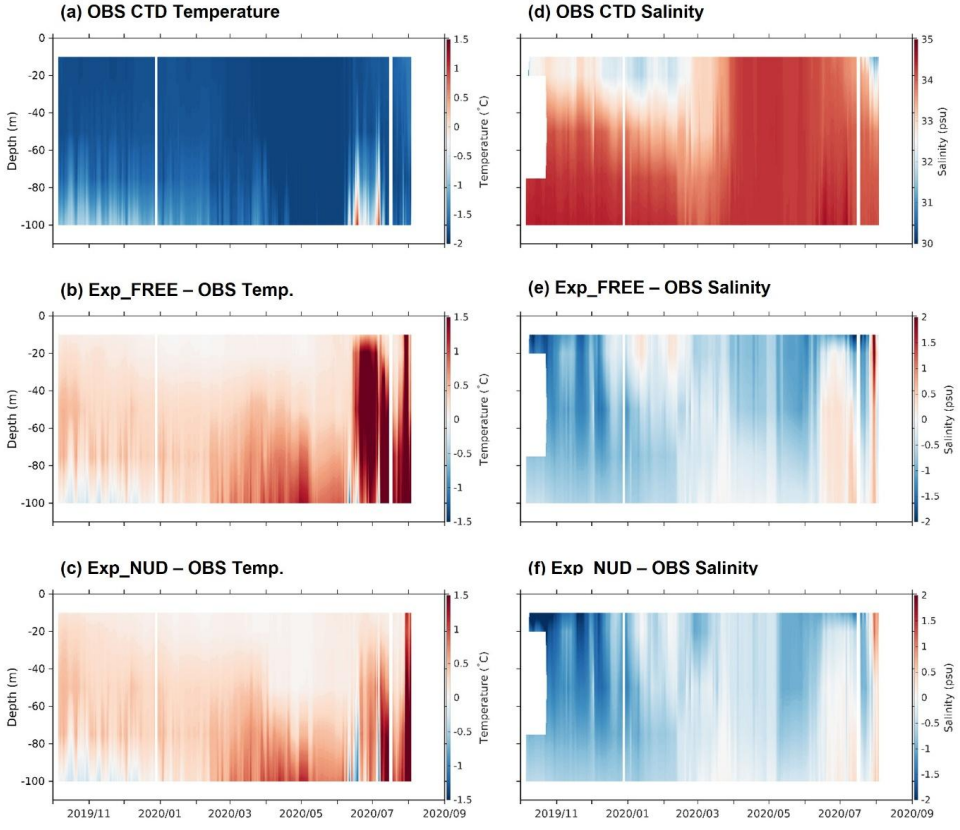

Figure 14 The evolutions of (a) oceanic temperature profile, and (d) salinity profile observed by the CTD buoys, and the temperature and salinity profile difference between the experiments and the observations for (b, e) Exp_FREE, and (c, f) Exp_NUD along the track of MOSAiC drift.

https://doi.org/10.5194/egusphere-2026-362
Preprint. Discussion started: 10 March 2026

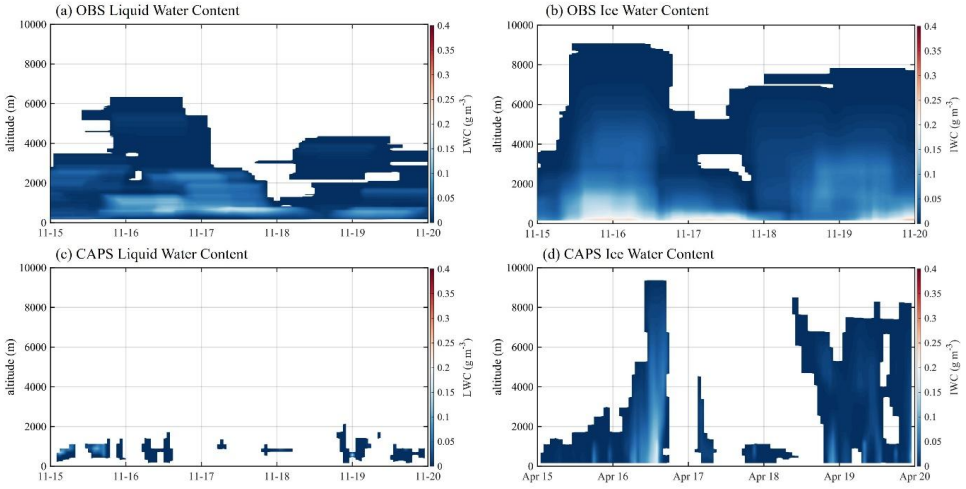

Figure 15 The evolutions of (a, c) liquid water content profile, and (b, d) ice water content profile for the observations and the model simulations during the STORM-1 period.